inorganics

MDPI

Review

Metal Complexes with Hydroxyflavones: A Study of Anticancer and Antimicrobial Activities

Ljiljana E. Mihajlović [1], Monica Trif [2] and Marijana B. Živković [3,*]

[1] Innovation Center of the Faculty of Chemistry, Studentski trg 12–16, 11158 Belgrade, Serbia; ljiljanam@chem.bg.ac.rs
[2] Centre for Innovative Process Engineering (CENTIV) GmbH, Boschstr. 8–10, 28857 Syke, Germany; monica_trif@hotmail.com
[3] Department of Chemistry, Institute of Chemistry, Technology and Metallurgy, National Institute of the Republic of Serbia, University of Belgrade, Studentski trg 12–16, 11000 Belgrade, Serbia
* Correspondence: marijana.zivkovic@ihtm.bg.ac.rs

Abstract

Metal chelation to bioactive small molecules is a well-established strategy to enhance the biological activity of the resulting complexes. Among the widely explored structural motifs, the combination of prominent metal centers with naturally inspired derivatives has attracted considerable attention. One such promising platform is the flavone scaffold, derived from flavonoids and studied since ancient times. Flavones are plant-derived compounds known for their diverse biological activities and health benefits. They exhibit significant structural variability, primarily through backbone modifications such as hydroxylation. Importantly, coordination of metal ions to hydroxylated flavone cores often improves their natural bioactivities, including anticancer and antimicrobial effects. In this review, we summarize transition metal complexes incorporating hydroxyflavone (OH–F) ligands reported over the past 15 years. We provide a concise overview of synthetic approaches and structural characterization, with a particular emphasis on coordination modes (e.g., maltol-type, acetylacetonate-type, catechol-type, and others). Furthermore, we discuss biological evaluation results, especially anticancer and antimicrobial studies, to highlight the therapeutic potential of these complexes. Finally, we suggest directions for the future development of metal-based agents bearing hydroxyflavone moieties through several critical points in terms of the accuracy, reproducibility, and relevance of biological studies involving metal-based compounds.

Keywords: transition metal complexes; flavonoid metal chelates; coordination mode; biological activity; cytotoxicity; antimicrobial

check for updates

Academic Editor: Claudio Pettinari

Received: 30 June 2025
Revised: 13 July 2025
Accepted: 18 July 2025
Published: 22 July 2025

Citation: Mihajlović, L.E.; Trif, M.; Živković, M.B. Metal Complexes with Hydroxyflavones: A Study of Anticancer and Antimicrobial Activities. *Inorganics* **2025**, *13*, 250. https://doi.org/10.3390/inorganics13080250

Copyright: © 2025 by the authors. Licensee MDPI, Basel, Switzerland. This article is an open access article distributed under the terms and conditions of the Creative Commons Attribution (CC BY) license (https://creativecommons.org/licenses/by/4.0/).

1. Introduction

According to the World Health Organization (WHO), cancer remains one of the leading causes of mortality, with nearly 10 million deaths reported worldwide in 2020, accounting for approximately one in six deaths [1]. The rapid mutation of cancer cells and the development of resistance to existing therapies represent major obstacles to effective treatment [2,3]. Furthermore, anticancer drugs often exhibit a limited selectivity for malignant cells over normal cells, resulting in systemic toxicity, adverse side effects, and damage to healthy tissues and organs.

Another pressing global health concern is the growing resistance to antimicrobial agents. The uncontrolled and excessive use of antibiotics may potentially return us to a

time when infectious diseases were frequently fatal due to the absence of effective treatment options [4].

One promising strategy to address both anticancer and antimicrobial resistance issues involves the rational design of novel compounds through the combination of different molecular fragments. Such an approach can lead to synergistic effects, improving therapeutic selectivity while minimizing toxicity. Notably, a substantial proportion of recently approved drugs are inspired by natural products and their structural motifs [5]. Evidence from the literature indicates that researchers have been investigating the therapeutic potential of metal complexes incorporating nature-inspired ligands, such as flavones, for several decades [6,7].

Flavones are natural compounds composed of three six-membered rings: two benzene rings (A and B) and a γ-pyrone ring (C). Benzene ring A is fused to the heterocyclic oxygen-containing ring C, while benzene ring B is attached to ring C at position C-2 (Figure 1).

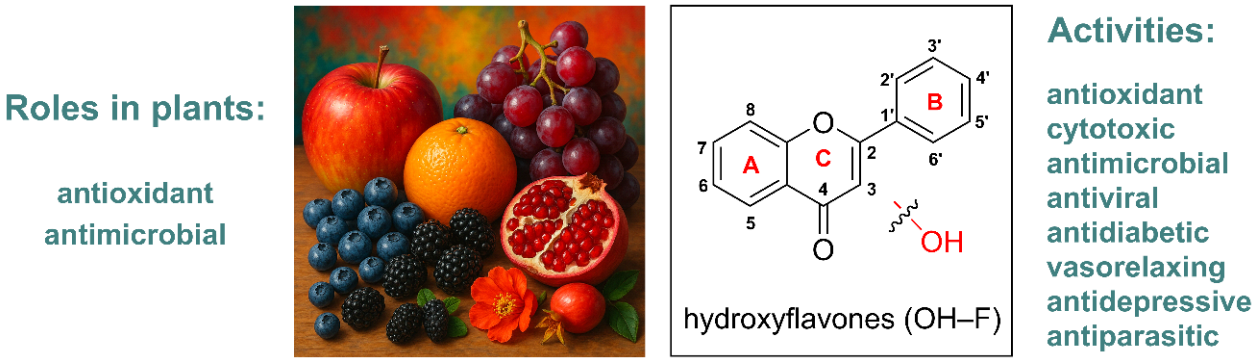


Figure 1. Origin of hydroxyflavones, their roles in plants, and associated biological activities.

Hydroxyflavones (OH–F) are characterized by the presence of one or more hydroxyl groups within their molecular structure. Figure 2 illustrates representative OH–F compounds selected from the scientific literature that will be examined in the present review.

OH–F are biosynthesized through the shikimate pathway, which ultimately leads to the formation of the aromatic amino acid phenylalanine (Figure 3). Phenylalanine is subsequently deaminated by phenylalanine ammonia-lyase (PAL) to yield cinnamic acid, which is hydroxylated by cinnamate-4-hydroxylase (C4H) to form p-coumaric acid. The activation of p-coumaric acid by 4-coumarate-CoA ligase (4CL) results in the formation of p-coumaroyl-CoA. This intermediate undergoes condensation with three molecules of malonyl-CoA, catalyzed by chalcone synthase (CHS), to generate chalcones. Chalcones are then isomerized to flavanones via chalcone isomerase (CHI), which are further oxidized by flavone synthase (FNS) to produce flavones. Subsequent hydroxylation of flavones at specific positions, mediated by cytochrome P450-dependent monooxygenases, leads to the formation of hydroxyflavones. A comprehensive overview of this biosynthetic pathway is provided in the review by Lou et al. [8].

OH–F play several essential roles in the plants that synthesize them. They function as effective antioxidants, safeguarding plant tissues from oxidative stress induced by UV radiation and environmental stressors [10]. Specific OH–F, such as chrysin and 3-hydroxyflavone, contribute to UV–B absorption, thus serving as natural sunscreens [11]. Furthermore, they are involved in plant defense mechanisms by exhibiting antimicrobial activity against bacterial and fungal pathogens [12]. Some hydroxyflavones also modulate plant–microbe interactions and influence auxin transport, thereby affecting plant growth and development [13].

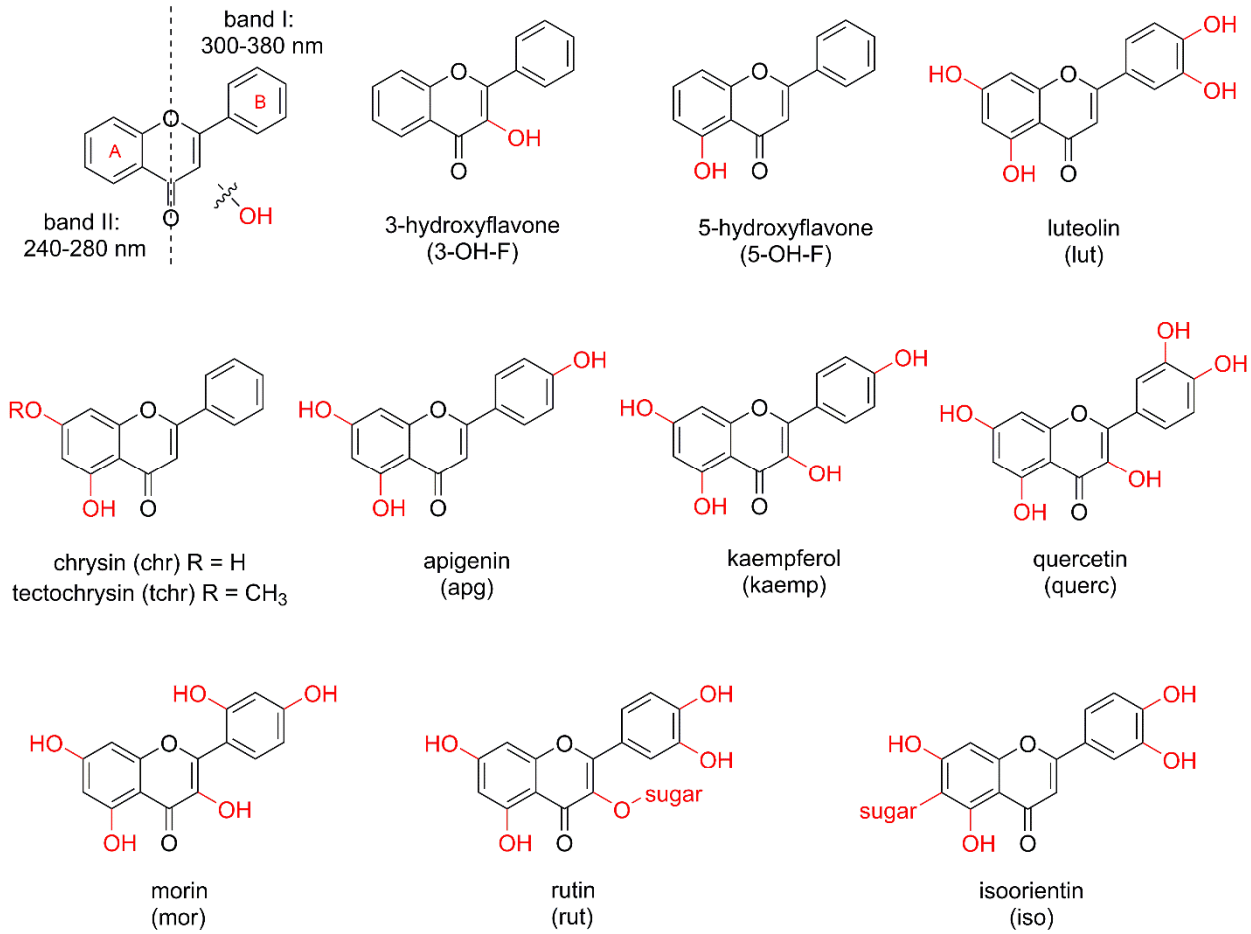


Figure 2. Characteristic UV–Vis absorption bands of hydroxyflavones [9], along with representative hydroxyflavone structures reported in the analyzed literature.

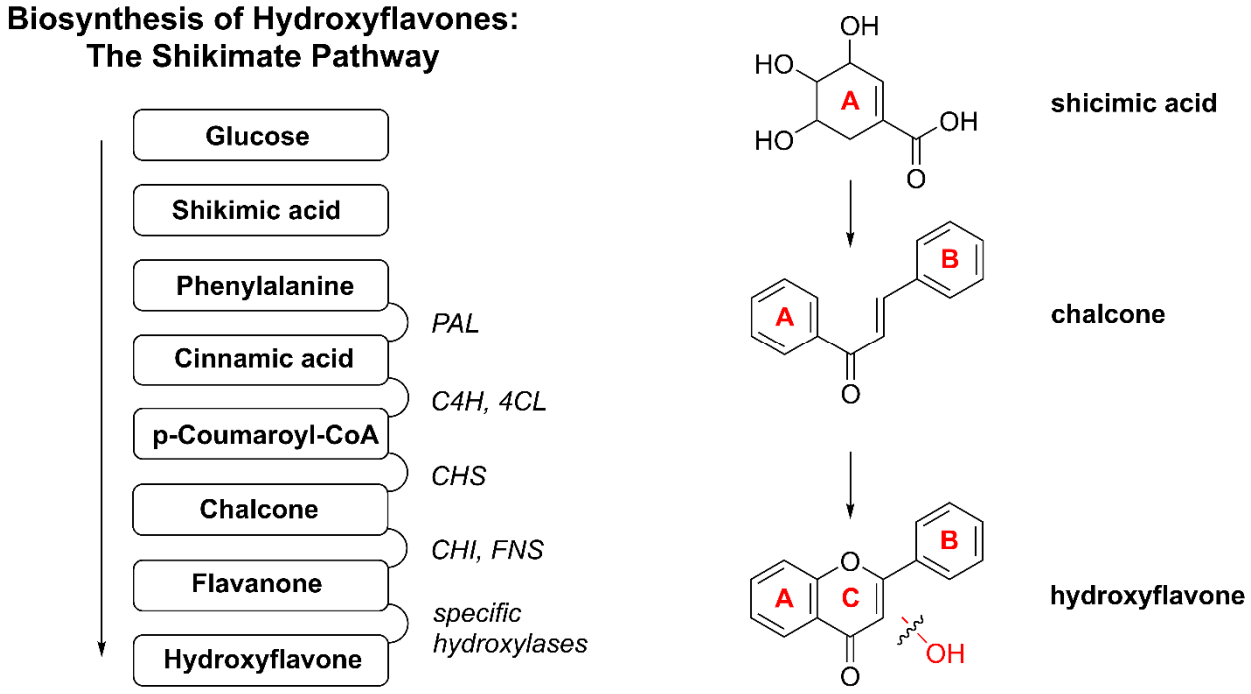


Figure 3. Biosynthetic pathway of hydroxyflavones derived from the shikimic acid route [8].

Over the past three decades, various biological activities of OH–F and its derivatives have been reported, including antioxidant [14–18], cytotoxic effects with distinct mechanisms of action [19–24], antimicrobial [18,25], antiviral [18], antidiabetic [26,27], vasorelaxant [28], antidepressant [29], antiparasitic [30], antiallergenic [31], and cholinesterase inhibitory activity [32].

This review focuses on transition metal complexes [M(OH–F)] featuring OH–F structural motifs, covering research published over the last 15 years. From a strictly chemical perspective, we outline common synthetic approaches used to obtain such compounds, highlight key techniques employed for their structural characterization, and discuss physicochemical properties relevant to biological applications, including stability and lipophilicity. The metal complexes are broadly categorized based on coordination modes, including maltol-type, acetylacetonate (acac)-type, catechol-type, mixed-type, and linear-type coordination.

Furthermore, their anticancer and antimicrobial activities are reviewed in the context of biological profiling. Ultimately, the aim of this review is to provide a comprehensive overview of recent advancements in this field and to underline how these findings may guide the development of next-generation anticancer and antimicrobial agents.

2. Metal–Hydroxyflavone Complexes and Their Biological Properties

In the coordination chemistry of OH–F, several commonly recognized bidentate (O,O) coordination modes to metal ions have been identified, including: (i) coordination via the 4-carbonyl and 3-hydroxyl groups (maltol-type, forming a five-membered chelate ring, see Section 2.1), (ii) coordination via the 4-carbonyl and 5-hydroxyl groups (acac-type, forming a six-membered chelate ring, see Section 2.2), (iii) coordination through two adjacent hydroxyl groups (catechol-type, five-membered chelate, see Section 2.3), and (iv) bridging coordination involving both acac- and catechol-type donor sites (see Section 2.4) (Figure 4). In addition to these bidentate modes, hydroxyflavones may also coordinate in a monodentate manner, as observed in some gold complexes (linear-type coordination, see Section 2.5) [33,34].

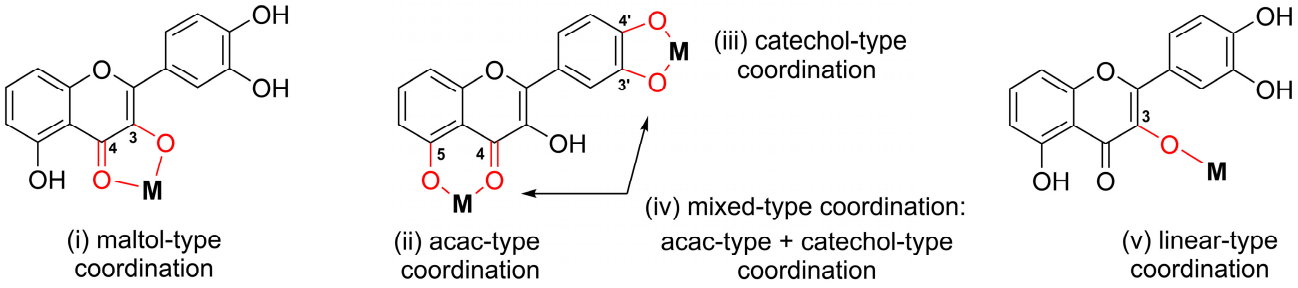


Figure 4. Representative coordination modes of OH–F to metal ions, including binding via: (i) the 4-carbonyl and 3-hydroxyl groups (maltol-type; forming a 5-membered chelate ring), (ii) the 4-carbonyl and 5-hydroxyl groups (acac-type; forming a 6-membered chelate ring), (iii) two adjacent hydroxyl groups (catechol-type; 5-membered chelate), (iv) mixed coordination involving both acac- and catechol-type donor sites, and (iv) only one hydroxyl group (linear-type).

Besides mononuclear complexes, which contain only one central metal ion, bi- and polynuclear complexes with hydroxyflavones have also been reported. However, recent studies have not identified any of these multinuclear complexes exhibiting anticancer or antimicrobial activity. Only a few examples of these complexes with mixed coordination and demonstrated biological activity will be discussed [35,36].

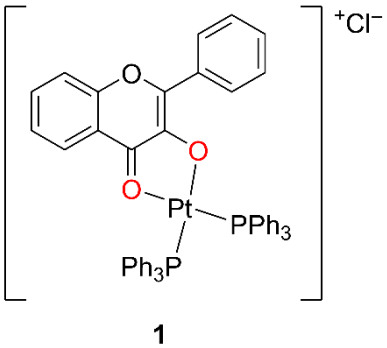
2.1. Maltol-Type Coordination

In metal complexes based on OH–F coordinated in a maltol-type manner, the ligand typically functions as a bidentate chelator, binding the metal center through two adjacent oxygen atoms located on the C-ring, namely the hydroxyl group at position C-3 and the carbonyl group at position C-4. This (O,O)-coordination mode results in the formation of a stable five-membered, envelope-like metallocycle, which critically influences the structural and electronic characteristics of the resulting complexes.

Coordination induces pronounced changes in the spectroscopic profiles of hydroxyflavones, which can be used to confirm a complex formation. In ultraviolet–visible (UV–Vis) spectra, band I, associated with a $\pi \rightarrow \pi^*$ transition involving the B-ring, typically undergoes a bathochromic shift of 10–30 nm upon metal coordination. In infrared (IR) spectra, the C=O stretching vibration (originally observed at 1650–1665 cm^{-1} in the free ligand) shifts to lower wavenumbers (around 1610–1630 cm^{-1}), while the broad O–H stretching band (3200–3500 cm^{-1}) diminishes or disappears, indicating deprotonation and coordination via the C-3 hydroxyl group. Additionally, new bands appear in the 400–600 cm^{-1} region, corresponding to metal–ligand vibrations. In ^{1}H NMR spectra, the disappearance of the characteristic signal for the hydroxyl proton at ~10–12 ppm further supports coordination, while the ^{13}C nuclear magnetic resonance (NMR) signal of the carbonyl carbon shifts downfield by a few ppm, consistent with metal binding.

2.1.1. (O,O)-Coordinated Complexes: Simple Metal–Hydroxyflavone Chelates

In 2016, Dell'Anna et al. synthesized three square-planar Pt(II) complexes bearing triphenylphosphine ligands and (O,O) bidentate donor ligands: 3-hydroxyflavone, quercetin, and ethyl gallate [37]. The complex containing ethyl gallate is not included in the present study. The complex with quercetin, coordinated in a catechol-type manner, is described in the following section, while complex **1** with 3-hydroxyflavone, exhibiting maltol-type coordination, is discussed here and shown in Figure 5. A concentrated methanolic solution of KOH was added dropwise to a dichloromethane solution containing equimolar amounts of *cis*-[$PtCl_2(PPh_3)_2$] and 3-hydroxyflavone under continuous stirring at room temperature. The reaction mixture was stirred overnight at an ambient temperature. The formed precipitate of KCl was removed by filtration, and the resulting filtrate was concentrated. Ethanol was added to the concentrated solution, followed by the addition of three equivalents of *n*-pentane, which induced the precipitation of an orange solid. The solid was isolated by filtration, washed with cold *n*-pentane, and dried under a vacuum.



1

Figure 5. Proposed structure of the platinum (II) complex with 3-hydroxyflavon (**1**), *cis*-[$Pt(PPh_3)_2$(3-OH–F)]Cl, as suggested by Dell'Anna et al. [37].

The structure of complex **1** was proposed based on data obtained from NMR and IR spectroscopy, high-resolution mass spectrometry (HRMS), and elemental analysis (EA). The coordination mode in the solution was elucidated by NMR spectroscopy, while in the

solid state it was determined using single-crystal X-Ray diffraction (XRD) analysis. The HRMS data supported the proposed molecular composition and structural formulation of the complex.

The single crystal obtained by slow diffusion of *n*-pentane into the tetrahydrofuran (THF) reaction solution was not of sufficient quality to allow complete structural refinement, likely due to the presence of photodegradation products. Upon standing in air, the complex gradually underwent photodegradation, yielding ortho-benzoyl-salicylic acid after five days, and subsequently, benzoic and salicylic acids upon prolonged exposure.

The cytotoxicity of complex **1** was evaluated using the 3-(4,5-dimethylthiazol-2-yl)-2,5-diphenyltetrazolium bromide (MTT) assay after 72 h of incubation against two tumor cell lines, U87 (human glioblastoma astrocytoma cell line), and MCF-7 (human breast adenocarcinoma cell line), without including any non-cancerous cell line to allow for the assessment of selectivity (Table 1). Cisplatin was not tested under the same experimental conditions; instead, the literature values were used for comparison. The cytotoxicity of free 3-OH–F and its platinum (II) complex **1** was found to be similar on the U87 cell line, indicating only a minor synergistic effect upon complexation. In contrast, on the MCF-7 cell line, the platinum complex exhibited approximately twice the cytotoxic activity of the free ligand. Overall, the cytotoxicity of the complex on both cell lines was significantly lower than that of cisplatin; however, due to the reliance on data from the literature for cisplatin, the validity of this comparison remains uncertain. Theoretical calculations support the observation that the platinum complex readily releases its coordinated bioactive ligand in the solution, implying that the biological activity of the complex may largely depend on the cytotoxicity of its leaving groups. Antimicrobial activity of the synthesized complex was not evaluated.

Table 1. Cytotoxicity of Pt(II) complex **1** determined by MTT assay after 72 h treatment against U87 (glioblastoma) and MCF-7 (breast) cancer cell lines. Data are mean values ± SD (n = 3) [37].

Compd.	IC_{50} (μM)	
	U87	MCF-7
***cis*-[$PtCl_2(PPh_3)2$]**	>200	>200
3-OH–F	27.5 ± 2.3	108.1 ± 3.5
1	26.3 ± 2.1	55.2 ± 1.7
Cisplatin [a]	1.76 ± 0.22	14 ± 3

[a] Reported from the literature.

In 2016, Raza and coworkers synthesized an octahedral complex of Fe(II) with quercetin, compound **2**, as presented in Figure 6 [38]. $FeSO_4 \cdot 7H_2O$ was refluxed and being stirred for 6 h with a double stoichiometric amount of quercetin in methanol. The reaction mixture was cooled, washed, and vacuum dried. The blackish-brown precipitate stable at room temperature was obtained.

The authors did not succeed in obtaining a crystal suitable for XRD analysis; therefore, the complex was characterized using other experimental techniques. Based on conductometric analysis (CA), complex **2** behaves as a nonelectrolyte, indicating its neutral nature. Two bidentately coordinated quercetin molecules and two water molecules are bound to a single Fe(II) ion. Upon addition of an Fe(II) salt to a methanolic solution of quercetin, a bathochromic shift in the UV–Vis absorption bands was observed, indicating a complex formation. The main changes in the IR spectrum upon complexation include a shift in the carbonyl stretching band from 1661 to 1646 cm^{-1}, and the appearance of a new band at 630 cm^{-1}, corresponding to Fe–O stretching. The presence of two water molecules in the complex was confirmed by both EA and thermogravimetric analyses (TGA). The absence of the NMR signal corresponding to the hydroxyl group at the C-3 position of quercetin

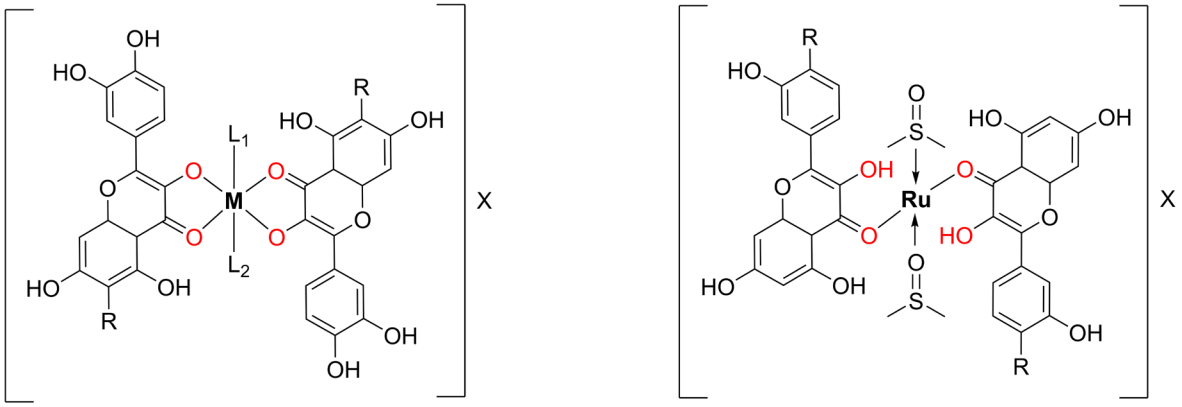
indicates a maltol-type coordination mode of quercetin to the Fe(II) ion. Additionally, scanning electron microscopy (SEM) of complex **2** revealed a uniform matrix morphology with ice rock-like surface structures, and the average particle size was approximately 5 µm.

The interaction of the quercetin–iron (II) complex **2** with deoxyribonucleic acid (DNA) was investigated using UV–Vis spectroscopy, fluorescence spectroscopy (FS), and agarose gel electrophoresis. The results indicated that the complex moderately intercalates into DNA, effectively quenches the fluorescence of the classical intercalator ethidium bromide (EB), and competes for intercalative binding sites. In addition, the complex was shown to cleave DNA via an oxidative mechanism. These findings suggest that the complex is capable of directly interacting with genetic material, which may underlie its cytotoxic effects and support its potential as an anticancer agent.

The antibacterial activity of the Fe(II) complex **2** was evaluated using the well diffusion method after 24 h of incubation against two bacterial strains: *Staphylococcus aureus* (Gram-positive, G+) and *Escherichia coli* (Gram-negative, G−) (Table 2). Penicillin sodium was used as the reference compound. The complex exhibited significantly stronger antibacterial activity compared to the free quercetin, as evidenced by larger inhibition zones, which may be explained by chelation theory [39]. The antibacterial effect of the complex was shown to be concentration dependent. The inhibition zones produced by complex **2** were 4–8 times wider than those observed for free quercetin, although still 2–3 times narrower than those produced by the reference compound.

Table 2. Antibacterial activity of the Fe(II) complex **2** evaluated using the well diffusion method. Zones of inhibition were measured in millimeters after 24 h of incubation [38].

Compd.	Zone of Inhibition (mm)			
	Staphylococcus aureus (G+)		*Escherichia coli* (G−)	
	1 mM	2 mM	1 mM	2 mM
Quercetin	0	1	1	3
2	5	7	8	11
Penicilin Sodium	14	15	16	19



2: M = Fe(II), R = H, L1 = L2 = H_2O, X = 1
3: M = Rh(III), R = H, L1 = H_2O, L2 = Cl, X = 1
4: M = Ru(II), R = OCH_3, L1 = S-dmso, L2 = O-dmso, X = 2 $NaNO_3$ × 2 H_2O
5: M = Ru(II), R = NO_2, L1 = S-dmso, L2 = O-dmso, X = 2 $NaNO_3$ × H_2O
6: M = Ru(II), R = Cl, L1 = S-dmso, L2 = O-dmso, X = 2 $NaNO_3$ × 5 H_2O

7: R = NMe_2; X = $(NO_3)_2$ × 2 H_2O

Figure 6. Proposed structures of Fe(II), Rh(III), and Ru(II) complexes with quercetin and its derivatives, as reported by Raza et al., Sahyon et al., and Singh et al., respectively [38,40,41].

In 2022, Sahyon et al. synthesized the Rh(III) complex **3** presented in Figure 3 by reacting quercetin with $RhCl_3 \cdot 3H_2O$ in an ethanolic NaOH solution under stirring at room temperature [40]. After the solvent was evaporated, a dark red microcrystalline complex precipitated. The product was then filtered, washed with an ethanol/diethyl ether (1:1) mixture, and dried under anhydrous conditions.

CA revealed that the quercetin-based Rh(III) complex **3** behaves as a non-electrolyte in the solution. TGA confirmed the presence of one water molecule in the coordination sphere of the complex, in agreement with the results of EA. The coordination mode was elucidated by comparing the IR spectra of free quercetin and the synthesized Rh(III) complex **3**. A shift in the carbonyl stretching frequency from 1664 cm^{-1} in free quercetin to 1620 cm^{-1} in complex **3** indicates the involvement of the carbonyl group in metal coordination. Among the hydroxyl groups, the C-3 hydroxyl was identified as the primary donor site due to its increased acidity attributed to its proximity to the carbonyl group and position within an oxygen-containing heterocyclic ring.

Rhodium(III) is a d^6 transition metal with an ^1A_1g ground state. In the synthesized complex **3**, the Rh(III) center adopts a hexa-coordinated, low-spin octahedral geometry, as evidenced by UV–Vis spectroscopy and magnetic susceptibility measurements. The diamagnetic character of the complex confirmed a $t_{2g}{}^6$ electron configuration, consistent with d^2sp^3 hybridization. Powder XRD (PXRD) analysis further supported this structure, showing similar bond lengths and bond angles close to 90°, indicating a quasi-ideal octahedral geometry. Good agreement was observed between the experimental PXRD data and theoretical calculations. The complex binds strongly to calf thymus DNA via a surface interaction with the phosphate backbone, inducing secondary structure changes ($Kb = 2.76 \times 10^6\ M^{-1}$), which may underlie its antiproliferative effect.

The cytotoxic potential of complex **3** was assessed using the MTT assay against five human cancer cell lines: cervical adenocarcinoma cell line (HeLa), hepatocellular carcinoma cell line (HepG2), colorectal adenocarcinoma cell line (Caco-2), prostate adenocarcinoma cell line (PC-3), and MCF-7 (breast), as well as one normal human lung fibroblast cell line (WI-38). Cisplatin was used as the reference drug (Table 3). In all tumor cell lines, complex **3** exhibited significantly higher cytotoxicity than free quercetin (4- to 15-fold); however, quercetin itself demonstrated markedly greater selectivity toward cancer cells. Compared to cisplatin, the complex was 2–4 times less cytotoxic but demonstrated an approximately 6-fold greater selectivity for cancer cells over normal cells. The highest selectivity indices (SI), calculated as the ratio of IC_{50} values for normal to tumor cells, were observed for HepG-2 (liver) and HeLa (cervix) cell lines, with values of 4.8 and 4.3, respectively.

Table 3. Cytotoxicity ($IC_{50} \pm$ SEM) of quercetin, the Rh(III) complex **3**, and cisplatin determined by MTT assay after 48 h of incubation [40].

Compd.	IC_{50} (μM)					
	HepG-2	**HeLa**	**MCF-7**	**PC-3**	**Caco-2**	**WI-38**
Quercetin	129.28 ± 13.5	68.78 ± 1.39	61.72 ± 3.29	91.92 ± 7.32	80.92 ± 9.04	454.5 ± 48.1
3	8.49 ± 0.40	9.40 ± 0.46	16.32 ± 0.81	17.71 ± 0.87	21.73 ± 1.13	40.58 ± 2.80
Cisplatin	4.50 ± 0.12	5.57 ± 0.23	4.17 ± 0.12	8.870 ± 0.635	12.49 ± 0.64	6.72 ± 0.29

Mechanistic studies suggest that complex **3** inhibits HeLa cell proliferation by inducing apoptosis, evidenced by cell cycle arrest in the pre-G1 phase, most likely due to inhibited DNA replication. This arrest may occur through the activation of the p53 tumor suppressor gene, as indicated by decreased levels of the anti-apoptotic Bcl-2 protein. Additionally, a reduction in MMP-9 levels was observed, supporting the complex's antiproliferative and anti-metastatic effects. Based on these findings, a mechanistic hypothesis can be

proposed: the complex **3** binds to the DNA surface, preventing replication in cancer cells and promoting p53 expression. Increased p53 levels can lead to the inhibition of both Bcl-2 and MMP-9, followed by the activation of caspase-9. Caspase-9 then activates caspase-3, initiating apoptosis. This apoptotic process results in the pre-G1 cell cycle arrest and decreased proliferation of HeLa cells, as reflected in the reduced proportion of cells in the G2/M phase.

To the best of our knowledge the antimicrobial activity of complex **3** was not investigated.

In 2017, Singh et al. synthesized a series of quercetin derivatives bearing para-substituted B-rings and subsequently prepared their [$Ru^{II}(DMSO)_2(querc)_2$] complexes (**4**–**7**, Figure 6) [41]. The distorted octahedral geometry structure of the complexes was proposed based on spectroscopic data (IR, NMR, and HRMS) and supported by density functional theory (DFT) calculations. In the resulting complexes **4**–**7**, two dimethyl sulfoxide (DMSO) ligands were coordinated monodentately, one via the sulfur atom and the other via the oxygen atom, reflecting the ambidentate nature of DMSO.

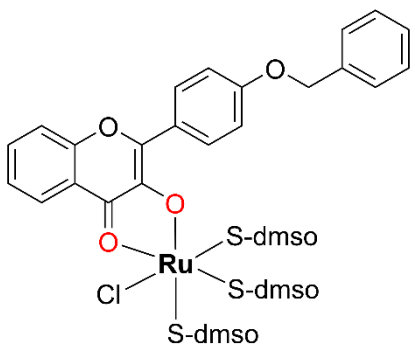
The cytotoxicity of the synthesized complexes **4**–**7** was evaluated using the MTT assay after 24 h of exposure against MCF-7 (breast) cell line (Table 4). Among the tested compounds, complex **4**, featuring a methoxy substituent on the B-ring, exhibited the highest cytotoxic activity against the MCF-7 cancer cell line (IC_{50} = 16 μM). In ligand–complex pairs, the IC_{50} values were consistently lower for the metal complexes **4**–**7** compared to their corresponding quercetin-based ligands, suggesting a potential synergistic effect between the metal center and the coordinated ligand.

Table 4. IC_{50} values of the synthesized complexes **4**–**7** determined by the MTT assay after 24 h of exposure [41].

Compd.	IC_{50} (μM)	Compd.	IC_{50} (μM)	Compd.	IC_{50} (μM)	Compd.	IC_{50} (μM)
	MCF7		MCF7		MCF7		MCF7
L4	17.2	**L5**	29.5	**L6**	38.4	**L7**	35.4
4	16.0	**5**	28.0	**6**	36.2	**7**	32.1

L4–**L7** are hydroxyflavone derivatives used as ligands in the corresponding complexes.

In 2010, Prajapati and coworkers synthesized two Ru(II) complexes with DMSO [42]. One of these complexes featured a chalcone ligand coordinated in a bidentate (O,O) fashion and is therefore not considered in this study. The other complex, compound **8**, which incorporates a 3-OH–F derivative, is relevant to the present discussion and is shown in Figure 7.



8

Figure 7. Structure of the Ru(II) complex **8**, *fac*-[RuCl(S-dmso)$_3$(3-OH–F)], containing a 3-OH–F derivative and coordinated DMSO ligands, as reported by Prajapati et al. [42].

The complex **8** was synthesized by the dropwise addition of a methanolic solution of *cis*-[$Ru^{II}Cl_2(dmso)_4$] to a methanolic solution of the 3-OH–F derivative containing an equimolar amount of Et_3N, adjusted to pH around 9.0. The resulting reaction mixture was stirred on a steam bath for 30 min. Subsequently, the solution was concentrated to one fourth of its original volume and left to stand at room temperature for 24 h. The resulting dark reddish-brown crystalline solid was collected by filtration, washed sequentially with methanol and diethyl ether, and finally dried under a vacuum. According to the authors, complex **8** is reported to be air-stable. CA indicates that it is a neutral species. The evidence for the complex **8** formation includes the appearance of a characteristic S=O stretching band around 1050 cm^{-1} and a Ru–S vibration band at approximately 430 cm^{-1}. The proposed structure of complex **8** was further confirmed by XRD analysis, which revealed a monoclinic crystal system containing four discrete complex molecules arranged in a chain, with no solvent-accessible voids in the crystal packing.

Preliminary cytotoxicity screening of complex **8** was performed using the MTT assay after 48 and 72 h of incubation against Dalton's lymphoma cell line, a murine transplantable T-cell lymphoma (DL) (Table 5). The IC_{50} value of complex **8** was found to be in the nanomolar range, indicating significantly higher cytotoxicity compared to the corresponding free OH–F ligand **L8**. This enhanced activity of complex **8** may suggest a synergistic effect between the coordinated ligand **L8** and the Ru(II) metal center in mediating the cytotoxic response.

Table 5. Cytotoxicity of complex **8** determined by MTT assay after 48 and 72 h of incubation against DL (lymphoma) cells [42].

Compd.	IC_{50} (μM)	
	48 h	**72 h**
DMSO control a	none	none
L8	>5	0.054
8	0.816	0.042

[a] DMSO was used as a vehicle control at 0.01% concentration. According to the original source, DL cells incubated with 0.01% DMSO alone did not produce any cytotoxicity.

Ruthenium–DMSO complexes have attracted considerable interest due to their promising selectivity toward solid tumor metastases and relatively low toxicity to healthy tissues [43], which has led some of these compounds to enter clinical trials [44].

In 2020, Gantsho and coworkers synthesized 18 Re(I) carbonyl complexes incorporating tropolone, 3-OH–F, and three differently substituted quinolones as bidentate ligands [45]. Since tropolone and quinolones are not members of the OH–F family, only five Re(I) tricarbonyl complexes **9**–**13** containing 3-OH–F will be discussed here (Figure 8). Starting from $[NEt_4]_2[Re(CO)_3Br_3]$, the addition of $AgNO_3$ at pH 2.2 yielded the triaqua complex *fac*-$[Re(CO)_3(H_2O)_3]^+$. Subsequent substitution of two labile aqua ligands with the bidentate 3-OH–F resulted in complex **9**. In methanolic solution, one of the coordinated water molecules is replaced by methanol, resulting in the complex **10**. Complexes **11**–**13** were synthesized by introducing one equivalent of a monodentate phosphine ligand. All complexes **9**–**13** were isolated as yellow precipitates or thin, needle-like crystals, which were unsuitable for XRD analysis. Structural characterization was performed using EA along with IR, UV–Vis, and NMR spectroscopy.

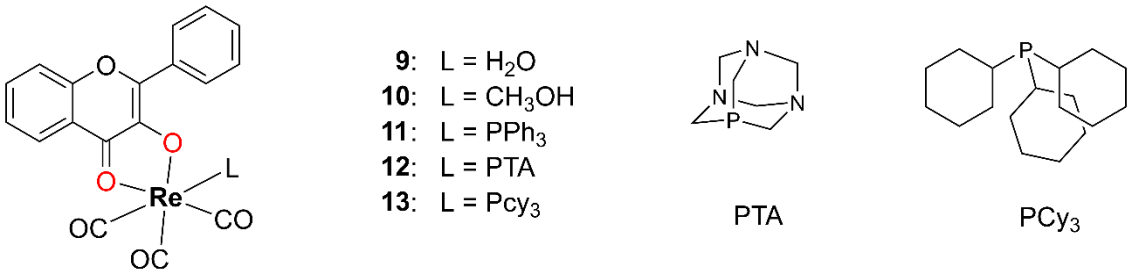


Figure 8. Proposed structure of the Re(I) tricarbonyl complexes **9**–**13** with 3-OH–F, as reported by Gantsho et al. [45].

Complexes **9** and **10** exhibit a high tendency toward the substitution of the coordinated water or methanol ligand. In complexes **11**–**13**, elevated temperatures and an excess of the phosphine ligand promote the efficient substitution of the axially positioned carbonyl ligand trans to the phosphine. The kinetics of the substitution of complex **10** with triphenylphosphine (PPh_3), 1,3,5-triaza-7-phosphaadamantane (PTA), and tricyclohexylphosphine (PCy_3) were studied, and all reactions proceeded via a single-step, first-order process, with rates directly dependent on the concentration of the entering phosphine ligand.

A cytotoxicity assessment was performed exclusively for complex **11** due to the limited solubility of the other complexes in this series. The evaluation employed a fluorometric cell viability assay based on resazurin after 48 h of incubation with HeLa (cervix) as the tumor cell line, and human retinal pigment epithelial cells immortalized with hTERT (RPE-1) as the normal cell line. Cisplatin served as a positive control (Table 6). The cytotoxicity of complex **11** against HeLa cells was comparable to that of cisplatin. The SI of the complex, calculated as the ratio of IC_{50} values for RPE-1 and HeLa cells, was 1.5, indicating a limited selectivity toward tumor cells under the tested conditions. In contrast, cisplatin exhibited an SI of approximately five. The authors suggest that the moderate cytotoxicity observed for complex **11** may be attributed to its high kinetic stability.

Table 6. Cytotoxicity of Re(I) complex **11**, *fac*-[$Re(CO)_3$(3-OH–F)(PPh_3)], determined by a fluorometric cell viability assay using resazurin after 48 h incubation. Results are expressed as IC_{50} values (μM). Cisplatin was used as a positive control [45].

Compd.	IC_{50} (μM)	
	HeLa	RPE-1
11	12.21 ± 0.17	18.41 ± 3.16
cisplatin	8.02 ± 0.57	39.07 ± 0.45

Kurzwernhart et al. synthesized 28 distinct metal complexes **14**–**41** derived from 3-OH–F derivatives with Ru(II), Os(II), and Rh(III) as metals [46–49]. The complexes adopt a pseudo-octahedral "piano-stool" geometry, characterized by slight variations in M–O bond lengths and a moderately twisted phenyl substituent on the ligand. The general structure of the complexes is presented in Figure 9, while the individual ligand structures and corresponding cytotoxicity data are summarized in Table 7. The cytotoxicity of complexes **14**–**41** was evaluated by an MTT assay after 96 h of exposure using three human cancer cell lines: the ovarian carcinoma cell line (CH1), the colorectal adenocarcinoma cell line (SW480), and the lung carcinoma epithelial cell line (A549). The positive control value for cisplatin was obtained from the literature.

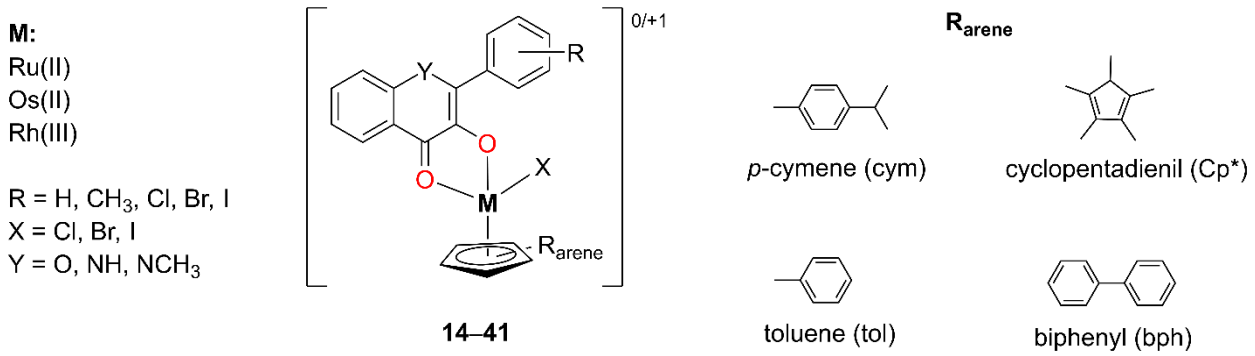


Figure 9. General structure of complexes **14–41** bearing 3-OH–F derivatives, as reported by Kurzwernhart et al. [46–49].

Table 7. Ligands of complexes **14–41** and their IC_{50} cytotoxicity values in CH1 (ovarium), SW480 (colon), and A549 (lung) cancer cell lines after 96 h exposure, determined by MTT assay (mean ± SD, n = 3) [46–49].

Compd.	X	Y	R	R_{arene}	M	IC_{50} ± SD (μM)			Ref. No.
						CH1 [a]	SW480	A549	
14	Cl	O	H	cym	Ru^{II}	2.1 ± 0.2	9.6 ± 1.5	20 ± 2	[46]
15	Cl	O	p-CH_3	cym	Ru^{II}	1.8 ± 0.2	7.2 ± 0.5	17 ± 2	[46]
16	Cl	O	p-F	cym	Ru^{II}	1.7 ± 0.4	7.9 ± 2.1	18 ± 1	[46]
17	Cl	O	p-Cl	cym	Ru^{II}	0.86 ± 0.06	3.8 ± 0.5	9.5 ± 0.5	[46]
18	Cl	O	m-F	cym	Ru^{II}	1.5 ± 0.1	7.0 ± 1.0	15 ± 1	[47]
19	Cl	O	o-F	cym	Ru^{II}	4.0 ± 0.8	24 ± 3	30 ± 1	[47]
20	Cl	O	m-Cl	cym	Ru^{II}	1.0 ± 0.1	7.0 ± 0.7	12 ±2	[47]
21	Cl	O	o-Cl	cym	Ru^{II}	7.9 ± 0.6	26 ± 1	51 ± 5	[47]
22	Cl	O	p-Br	cym	Ru^{II}	1.2 ± 0.2	3.4 ± 0.1	8.6 ± 0.7	[47]
23	Cl	O	m-Br	cym	Ru^{II}	2.3 ± 0.7	7.2 ± 0.4	17 ± 3	[47]
24	Br	O	H	cym	Ru^{II}	2.8 ± 0.4	12 ± 1	27 ± 4	[48]
25	Br	O	p-Cl	cym	Ru^{II}	0.86 ± 0.04	3.4 ± 0.4	7.9 ± 0.6	[48]
26	I	O	H	cym	Ru^{II}	1.6 ± 0.2	9.6 ± 1.5	16 ± 1	[48]
27	I	O	p-Cl	cym	Ru^{II}	1.2 ± 0.3	4.7 ± 0.9	8.9 ± 0.8	[48]
28	Cl	O	H	tol	Ru^{II}	3.2 ± 0.1	12 ± 3	19 ± 1	[48]
29	Cl	O	p-Cl	tol	Ru^{II}	0.88 ± 0.17	4.7 ± 0.6	7.8 ± 2.5	[48]
30	Cl	O	H	bph	Ru^{II}	5.5 ± 1.2	9.2 ± 1.9	28 ± 5	[48]
31	Cl	O	p-Cl	bph	Ru^{II}	6.3 ± 1.1	21 ± 4	59 ± 1	[48]
32	Cl	N-H	H	cym	Ru^{II}	4.0 ± 0.2	14 ± 1	17 ± 2	[48]
33	Cl	N-CH_3	H	cym	Ru^{II}	5.3 ± 0.2	12 ± 2	19 ± 1	[48]
34	Cl	O	H	cym	Os^{II}	2.5 ± 0.2	12 ± 1	16 ± 1	[49]
35	Cl	O	p-CH_3	cym	Os^{II}	0.58 ± 0.06	6.6 ± 0.2	4.8 ± 1.0	[49]
36	Cl	O	p-F	cym	Os^{II}	1.7 ± 0.2	7.6 ± 0.1	16 ± 2	[49]
37	Cl	O	p-Cl	cym	Os^{II}	0.90 ± 0.06	4.2 ± 0.3	8.0 ± 0.5	[49]
38	Cl	O	H	Cp*	Rh^{III}	3.1 ± 0.3	7.9 ± 0.8	15 ± 3	[49]
39	Cl	O	p-CH_3	Cp*	Rh^{III}	2.0 ± 0.2	6.3 ± 0.8	11 ± 3	[49]
40	Cl	O	p-F	Cp*	Rh^{III}	2.0 ± 0.1	7.6 ± 0.6	13 ± 4	[49]
41	Cl	O	p-Cl	Cp*	Rh^{III}	1.0 ± 0.0	2.5 ± 0.8	4.3 ± 1.8	[49]
CDDP [b]	-	-	-	-	-	0.14 ± 0.03	3.3 ± 0.4	1.3 ± 0.4	[46]

[a] It was the CH1/PA-1 cell line for compounds **34–41**. [b] Literature-reported data.

Complexes **14–23**, with the general formula [Ru^{II}(Cl)(cym)(3-OH–F)], differ in both the nature and position of substituents on the B-ring of the 3-OH–F scaffold. For several of these complexes (**15**, **17**, **18**, and **21**), single-crystal XRD data were obtained. Complexes bearing

para-substituted B-rings exhibited the highest cytotoxic activity. In contrast, the reduced activity observed for ortho-substituted derivatives may be attributed to steric effects, as the phenyl ring in these compounds adopts a significantly more twisted conformation. This structural distortion is likely to impair molecular recognition and diminish the binding affinity to biological targets. Notably, all complexes showed a stronger inhibition of topoisomerase IIα compared to the corresponding free OH–F derivatives, which was attributed to their multitargeted mechanism of action. Furthermore, the extent of topoisomerase IIα inhibition correlated well with the observed cytotoxicity.

In a subsequent set of compounds (**24–33,** $[Ru^{II}(X)(R_{arene})(3\text{-OH–F})]$), the aromatic ligand coordinated to the metal center (R_{arene}) was varied. The results showed that changes in lipophilicity were more strongly influenced by the 3-OH–F ligand than by the R_{arene} moiety [40]. Finally, in complexes **34–41**($[Os^{II}/Rh^{III}(Cl)(R_{arene})(3\text{-OH–F})]^{0/+1}$), ruthenium (II) was replaced by osmium (II) or rhodium (III) as the central metal ion, but this did not significantly alter the observed cytotoxicity [41].

The complexes **14–41** synthesized by Kurzwernhart et al. exhibited the highest cytotoxic activity against the CH1 (ovarian) cell line, while lower activity was observed against the SW480 (colon) and the lowest toward A549 (lung) cells, which are generally more resistant. Most IC_{50} values for the CH1 cell line were in the low micromolar range (≤7.9 μM), with compounds **17**, **25**, **29**, **35**, and **37** showing nanomolar potency. These five compounds share structural features including a chloride leaving group and a para-substituted B-ring of the OH–F moiety bearing either a chlorine or methyl substituent. These results suggest that both the nature and position of substituents on the B-ring, as well as the identity of the leaving group, play a critical role in enhancing cytotoxicity.

2.1.2. Mixed-Ligand Systems: Incorporating Both (O,O) and (N,N) Donor Atoms

Starting from *cis*-$[Ru^{II}(bpy)_2Cl_2]$ or $[Ru^{II}(phen)_2(CO_3)]$, Zahirović et al. synthesized a series of octahedral cationic ruthenium (II) complexes **42–47** with OH–F ligands [50]. In these complexes, the diimine ligands, 2,2′-bipyridine (bpy) or 1,10-phenanthroline (phen), are coordinated in a bidentate manner through nitrogen atoms, while the OH–F ligand is coordinated via two oxygen atoms in a maltol-type binding mode (Figure 10). The resulting complexes are low-spin, diamagnetic species consistent with a t_{2g}^6 electronic configuration of the Ru(II) center.

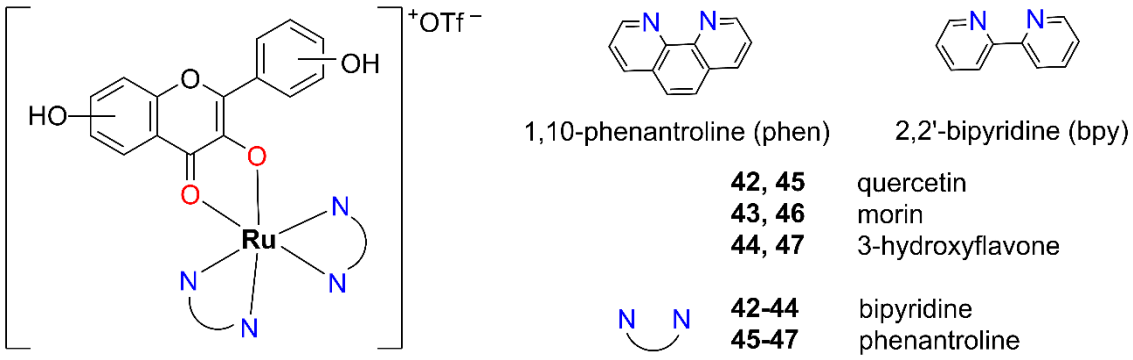


Figure 10. Proposed structures of the synthesized heteroleptic $[Ru^{II}(phen/bpy)_2(OH–F)]OTf{\cdot}nH_2O$ complexes **42–47**, as reported by Zahirović et al. [50].

Given that the synthesized complexes **42–47** lack good leaving groups, the most probable mode of DNA interaction is intercalation. This is supported by their cationic nature and the presence of planar π-extended aromatic systems. On the other hand, the efficiency of π–π stacking interactions with nucleobases tends to decrease with the increasing number of hydroxyl groups on the OH–F ligand.

The cytotoxicity of these types of Ru(II) complexes **42**–**47** was evaluated using the MTT assay after 72 h of incubation on four human cancer cell lines: colorectal adenocarcinoma cell line (SW620), HepG2 (liver), MCF-7 (breast), and HeLa (cervix) (Table 8). Unfortunately, the measurement errors were sufficiently high enough to raise concerns regarding the reliability and significance of the obtained results. However, two results stood out as significant: the bipyridine-based complex **44** exhibited nanomolar cytotoxicity against SW620 cells (IC_{50} = 0.75 μM), while the phenanthroline-based complex **47** showed micromolar activity against the MCF-7 cell line (IC_{50} = 8.32 μM). Both of these complexes are derivatives of 3-OH–F.

Table 8. Cytotoxicity of complexes **42**–**47** determined by MTT assay after 72 h treatment expressed as (mean ± SD, n = 3) [50].

Compd.	IC_{50}			
	SW620	**HepG-2**	**MCF-7**	**HeLa**
quercetin	>100	59.54 ± 20.48	>100	93.22 ± 22.97
morin	>100	>100	>100	>100
3-OH–F	50.73 ± 22.29	8.88 ± 17.68	42.06 ± 21.08	5.44 ± 31.22
***cis*-[Ru(bpy)$_2$Cl$_2$]·2H$_2$O**	4.53 ± 60.11	>100	2.10 ± 70.64	>100
[Ru(phen)$_2$(CO$_3$)]·2H$_2$O	>100	>100	92.38 ± 44.00	>100
42	>100	>100	0.39 ± 70.64	>100
43	>100	>100	85.87 ± 70.64	>100
44	0.75 ± 0.15	2.51 ± 0.67	0.52 ± 0.38	0.78 ± 0.20
45	>100	>100	>100	>100
46	>100	>100	7.64 ± 70.43	>100
47	8.23 ± 46.41	11.42 ± 66.02	8.32 ± 0.86	19.32 ± 65.89

Antimicrobial activity was assessed by the disk diffusion method against four Gram-positive bacterial strains (*Staphylococcus aureus* ATCC 25923, *Enterococcus faecalis* ATCC 19433, *Streptococcus* β-hemolytic group A, and methicillin-resistant *Staphylococcus aureus* (MRSA)). Vancomycin was used as the reference drug for all Gram-positive strains, except for MRSA, where gentamicin served as the control. Four Gram-negative bacterial strains were also tested (*Klebsiella pneumoniae* ATCC 1705, *Acinetobacter baumannii* ATCC BAA-747, *Pseudomonas aeruginosa*, and *Escherichia coli*), with gentamicin as the reference drug. Additionally, the fungal strain *Candida albicans* was included, with nystatin used as the control. The results are presented in Table 9. Interestingly, complex **44** exhibited zones of inhibition against Gram-positive bacteria comparable in width to that of vancomycin. In the case of MRSA, the zone of inhibition was significantly wider than that of gentamicin. Against the tested fungal strain, the inhibition zone observed for **44** was identical to that measured for nystatin. Comparison of the inhibition zones of the synthesized metal complexes with those of the free hydroxyflavone ligands indicates a synergistic effect of coordination, enhancing antimicrobial activity against both Gram-positive bacteria and the fungal strain *Candida albicans*. Based on the obtained results, a significant improvement in the antimicrobial efficacy of complex **44** was observed against the tested Gram-positive bacteria and *Candida albicans* strains, relative to the uncoordinated 3-hydroxyflavone ligand.

Table 9. Antimicrobial activity of free 3-OH–F and its ruthenium (II) complex [Ru(bpy)$_2$(3-OH–F)](OTf)·nH$_2$O **44**, evaluated by the disk diffusion method and expressed as inhibition zone diameters (mm) [50].

Compd.	*Staphylococcus aureus* ATCC 25923	*Enterococcus faecalis* ATCC 19433	*Streptococcus* Beta-Hemolytic Group A	Methicillin-Resistant *Staphylococcus aureus*	*Klebsiella pneumoniae* ATCC 1705	*Acinetobacter baumannii* ATCC—BAA 747	*Pseudomonas aeruginosa*	*Escherichia coli*	*Candida albicans*
	G+	G+	G+	G+	G−	G−	G−	G−	Fungus
	Diameter of Inhibition Zone (mm)								
3-OH–F	*	*	*	12	*	16.5	*	*	18.5
44	25	20	20	26	*	16	13	*	28
vancomycin	27	26	35	-	-	-	-	-	-
gentamicin	-	-	-	20	25	35	36	21	-
nystatin	-	-	-	-	-	-	-	-	28

* No activity, - not tested, G+ = Gram-positive bacteria, and G− = Gram-negative bacterial strain.

Gençkal et al. synthesized heteroleptic complexes of Co(II), Ni(II), and Cu(II) with quercetin and diimine (phen or bpy) ligands (**48**–**51**, Figure 11) [51]. A methanolic solution of metal (II) chloride x-hydrate was added dropwise to a methanolic solution of quercetin and sodium hydroxide under constant stirring at room temperature. The reaction mixture was stirred for an additional hour, after which a methanolic solution of phen or bpy was added. The mixture was then refluxed for approximately 4 h. Upon completion, it was allowed to cool to room temperature, and the resulting solid was filtered, washed with methanol, and dried under ambient conditions.

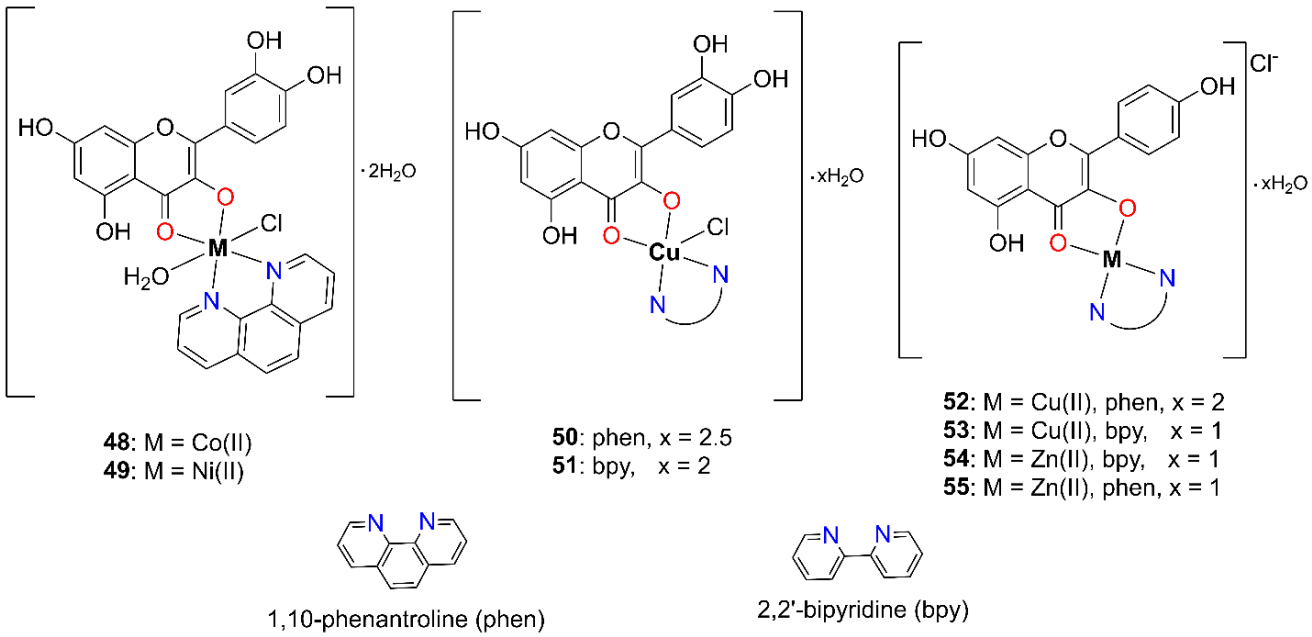


Figure 11. Proposed structures of M(II) complexes with quercetin (**48**–**51**) or kaempferol (**52**–**55**), as suggested by Gençkal et al. and Wang et al., respectively [51,52].

According to experimental measurements, two distinct types of complexes were obtained: an octahedral [Co^{II}/Ni^{II}(queH-1)Cl(phen)(H$_2$O)]·2H$_2$O (**48**–**49**), and a square-pyramidal geometry for [Cu^{II}(queH-1)Cl(phen/bpy)]·xH$_2$O (**50**–**51**), as illustrated in Figure 11.

EA confirms the proposed molecular formulas of the complexes **48**–**51**. CA indicates that the complexes are neutral in nature and thus behave as non-electrolytes. Their stability was verified by repeating the CA after 24 and 48 h, with consistent results. The magnetic susceptibility (χ) values for the Ni(II) and Co(II) complexes are consistent with mononuclear

octahedral coordination, while those for the Cu(II) complexes support the assignment of a mononuclear square-pyramidal geometry for complexes **50** and **51**. In the UV–Vis spectrum, the characteristic absorption band of free quercetin at 371 nm, assigned to the B-ring, undergoes a bathochromic shift of approximately 50 nm upon complexation, supporting a maltol-type coordination mode of the quercetin ligand. The band maximum corresponding to the carbonyl stretching vibration shifted to lower wavenumbers in all metal complexes, indicating coordination through the adjacent hydroxyl group. Since the hydroxyl group at the C3 position is significantly more acidic than the one at C5, it is expected to preferentially participate in metal coordination. Furthermore, the IR spectra reveal new bands in the 433–417 cm^{-1} and 652–643 cm^{-1} regions, corresponding to M–N and M–O bond vibrations, respectively, confirming the formation of metal–ligand bonds through nitrogen and oxygen donor atoms.

The cytotoxic activity of the compounds **48**–**51** was initially evaluated using Sulforhodamine B (SRB) and ATP-based cell viability assays after 48 h of incubation against four different human cancer cell lines: A549 (lung), PC-3 (prostate), HeLa (cervix), and MCF-7 (breast). Improved results were obtained using the ATP assay, which is generally more sensitive than the SRB assay. Among them, the Cu(II) complexes **50** and **51** exhibited the most pronounced cytotoxicity toward the MCF-7 breast cancer cell line. Consequently, an additional breast cancer cell line, namely the human triple-negative breast cancer cell line (MDA-MB-231), was selected for further evaluation. At higher concentrations, some cytotoxic activity was also observed for the free ligands, quercetin, phen, and bpy, in breast cancer cell lines, although this activity was significantly lower compared to that of the Cu(II) complexes. Complex **50**, containing phen, showed high cytotoxicity after 48 h of exposure in both MCF-7 and MDA-MB-231 cell lines, with IC_{50} values in the low micromolar range. One of the mechanisms underlying the cytotoxic effect of complex **50** was identified as apoptosis induction, as evidenced by an approximately 40% increase in apoptotic cells, mediated through the Caspase-3/7-dependent pathway. These findings identify complex **50** as a promising candidate for further development as an antitumor agent targeting breast cancer.

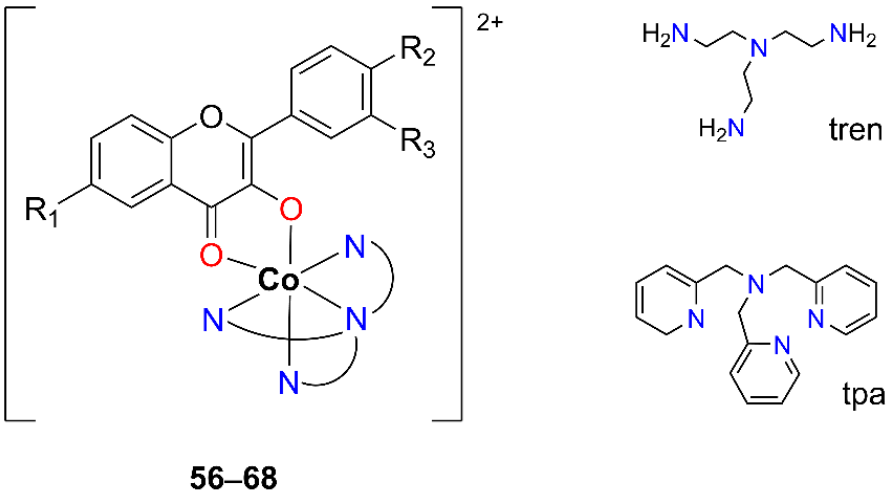
In 2014, Wang et al. synthesized four M(II) complexes **52**–**55** (M = Cu(II) or Zn(II)) incorporating the OH–F kaempferol as an (O,O) donor ligand, along with bpy or phen as (N,N) donor ligands, as depicted in Figure 11 [52]. A methanolic solution of MCl_2 was added to a methanolic solution containing equimolar amounts of kaempferol and NaOH at an ambient temperature. Subsequently, bpy or phen, dissolved in methanol, was added dropwise. The reaction mixture was filtered, and the resulting yellow precipitate was washed with ethanol and dried under a vacuum. Since single crystals suitable for XRD analysis could not be obtained, the structures of the complexes were proposed based on EA, HRMS, UV–Vis, IR, and NMR spectroscopy. A fluorometric competitive experiment using EB as a probe revealed moderate intercalation by the complexes. The increased viscosity of CT-DNA in the presence of the metal complexes **52**–**55** further supported these findings. Notably, the complexes **52**–**55**, especially complex **52**, were able to induce the cleavage of plasmid DNA (pUC19) in a dose-dependent manner.

Kaempferol and its complexes (**52**–**55**) were tested for cytotoxic activity against the MDA-MB-231 (breast) cancer cell line using the MTT assay after 24 h of incubation (Table 10). All complexes showed significantly improved cytotoxicity compared to the free ligand, indicating a potential synergistic interaction between kaempferol and the coordinated metal ions.

Table 10. Cytotoxic activity of metal complexes **52**–**55** with kaempferol against MDA-MB-231 cells, determined by MTT assay after 24 h of treatment. Data are expressed as mean ± SD (n = 3) [52].

Compd.	IC_{50} (μM)
	MDA-MB-231
kaempferol	39.76 ± 1.06
52	17.39 ± 1.42
53	23.71 ± 1.12
54	29.89 ± 1.19
55	27.49 ± 1.42

In 2021, Kozsup et al. reported the synthesis and characterization of a series of sixteen octahedral Co(III) complexes containing derivatized OH–F and tetradentate nitrogen ligands [53], namely tris(2-aminoethyl)amine (tren) or tris(2-pyridylmethyl)amine (tpa). Thirteen compounds of these (**56**–**68**, $[Co^{III}(4N)(OH–F)]^{2+}$) were obtained by maltol-type coordination (Figure 12, Table 11), using variously substituted OH–F-ligands (3-hydroxyflavone (flavH), 6-F-3′-NO_2-3-hydroxyflavone (NO_2FflavH), 3′-NO_2-3-hydroxyflavone (NO_2flavH), 4′-Me-3-hydroxyflavone (MeflavH), 6-Cl-4′-OMe-3-hydroxyflavone (ClO-MeflavH), 6-Br-3-hydroxyflavone (BrflavH), and 4′-iPr-3-hydroxyflavone (iPrflavH). Two additional complexes (**69** and **70**, Figure 13) were obtained by the acac method and will be discussed in the following Section 2.2. One complex, ([Co(tren)(nar)](Cl)(ClO_4)), which contains naringenin (nar) from the flavanone family, will not be a subject of this review.



56–68

Figure 12. The chemical structures of Co(III) complexes **56**–**68** with differently substituted OH–F obtained by maltol-type coordination, as reported by Kozsup et al. [53].

The $[Co(4N)(flav)]^{2+}$ type of compounds (**56**–**70**) was obtained in an overnight reaction by mixing the stoichiometric amount of the metal precursor ($[Co(4N)Cl_2]Cl$ (4N = tren or tpa)) and the ligand in MeOH at 60 °C with an equivalent of NaOH as a base. Most of the complexes were crystallized from water solutions after the addition of a counterion, ClO_4^-.

Table 11. Numeration of Co(III) complexes **56**–**68** bearing different OH–F derivatives [53].

Compd.	Abbreviation	4N	R_1	R_2	R_3
[Co(tren)(flav)]$(ClO_4)_2$	**56**	tren	-	-	-
[Co(tpa)(flav)]$(ClO_4)_2$	**57**	tpa	-	-	-
[Co(tren)(Brflav)]$(ClO_4)_2$	**58**	tren	Br	-	-
[Co(tpa)(Brflav)]$(ClO_4)_2$	**59**	tpa	Br	-	-
[Co(tren)(Meflav)]$(ClO_4)_2$	**60**	tren	-	Me	-
[Co(tpa)(Meflav)]$(ClO_4)_2$	**61**	tpa	-	Me	-
[Co(tren)(NO_2Fflav)]$(ClO_4)_2$	**62**	tren	F	-	NO_2
[Co(tpa)(NO_2Fflav)]$(ClO_4)_2$	**63**	tpa	F	-	NO_2
[Co(tren)(NO_2flav)](Cl)(ClO_4)	**64**	tren	-	-	NO_2
[Co(tpa)(NO_2flav)]$(ClO_4)_2$	**65**	tpa	-	-	NO_2
[Co(tren)(ClOMeflav)]$(ClO_4)_2$	**66**	tren	Cl	OMe	-
[Co(tren)(iPrflav)]$(ClO_4)_2$	**67**	tren	-	iPr	-
[Co(tpa)(iPrflav)]$(ClO_4)_2$	**68**	tpa	-	iPr	-

The full characterization of a series of compounds **56**–**70** included NMR, IR, and HRMS measurements, as well as crystal structure and a cyclic voltammetric (CV) analysis. Characterization data confirmed acac coordination mode (O,O) of the OH–F ligand to the metal ion and octahedral geometry in all cases. Prior to biological study, the Co(III) species were tested for their stability in a D_2O:DMSO = 5:1 (v/v) mixture revealing no spectral changes in ambient conditions. Additionally, their electrochemical profile was determined using CV. The redox study indicated the influence of the substituents on the values of reduction potential as the presence of electron-donating substituents on the OH–F further shifted the cobalt complex's reduction potential toward more negative values. The nature of the substituents demonstrated the greatest impact on the cytotoxic activity of the compounds (Table 11).

The cytotoxicity of most complexes (**56**–**65**), as well as the free flavone ligands, was evaluated after 72 h of incubation against two human cancer cell lines, epithelial carcinoma cell line (A431) and A549 (lung), under both normoxic (21% O_2) and hypoxic (1% O_2) conditions and end-point SRB assay (Table 12). The A549 cell line was generally more sensitive to the tested compounds than A431, with the exception of compound **60**, for which the EC_{50} values were lower in the A431 cells. Among the free ligands, MeflavH exhibited no cytotoxicity against either cell line, while flavH showed slight activity only against A549 under normoxic conditions. The ligands NO_2flavH, NO_2FflavH, and BrflavH were also exclusively active against A549, but their cytotoxic effects in this cell line were significant. Overall, the results indicate that the Co(III) species derived from the [Co(tpa)Cl_2]Cl precursor exhibit significantly stronger cytotoxic effects compared to those obtained from [Co(tren)Cl_2]Cl, highlighting the influence of substituent variation in OH–F-based ligands.

Table 12. Studied Co(III) complexes **56**–**65** obtained by maltol-type coordination and their cytotoxicity against A549 and A431 human cancer cell lines under normoxic and hypoxic conditions after 72 h incubation using end-point SRB assay. EC_{50} and 95% confidence interval (CI) values are presented in μM as a mean of three independent experiments [53].

Compd.	EC_{50}(μM)			
	A431		A549	
	Normoxia	Hypoxia	Normoxia	Hypoxia
[Co(tren)Cl_2]Cl	>100	>100	>100	>100
[Co(tpa)Cl_2]Cl	>100	>100	>100	>100
flavH	>100	>100	36	>100

Table 12. *Cont.*

Compd.	EC_{50}(μM)			
	A431		A549	
	Normoxia	Hypoxia	Normoxia	Hypoxia
MeflavH	>100	>100	>100	>100
BrflavH	84 [+29, −19]	>100	7.0 [+1, −1]	12 [+7, −4]
NO_2flavH	64 [+7, −6]	>100	15 [+3, −2]	17 15 [+3, −3]
NO_2FflavH	>100	>100	16 15 [+2, −2]	15 15 [+3, −2]
56	>100	>100	>100	>100
57	45 [+4, −3]	47 [+7, −6]	8.3 [+1.2, −1.1]	21 [+3, −4]
58	55 [+11, −9]	91 [+39, −23]	89 [+12, −12]	73 [+20, −16]
59	13 [+2, −2]	17 [+2, −2]	6.8 [+1.0, −0.8]	8.9 [+3.6, −2.9]
60	44 [+5, −4]	88 [+15, −12]	>100	>100
61	17 [+3, −2]	26 [+4, −4]	14 [+1, −1]	17 [+11, −7]
62	>100	>100	72 [+15, −12]	48 [+8, −7]
63	15 [+3, −2]	22 [+4, −3]	5.2 [+0.7, −0.6]	6.9 [+1.2, −1.1]
64	n.e.	n.e.	n.e.	n.e.
65	14 [+4, −3]	23 [+5, −4]	6.3 [+1.0, −0.9]	7.3 [+1.3, −1.4]
cisplatin	3.2 [+0.7, −0.6]	5.6 [+1.3, −1.1]	1.8 [+0.2, −0.2]	2.4 [+0.7, −0.6]

n.e.—not evaluated; the original study did not provide a reason.

2.2. Acac-Type Coordination

The second part of our review study will focus on the acetylacetone (2,4-pentanedione, acac) type of coordination using the common acac ligand platform in coordination chemistry. Acac's ubiquity originates from its stability, easy synthesis, and the chelate effect. Typical acac chemistry relies on two types of reactions: (a) conversions with Lewis bases when acac coordinates via both oxygens; (b) electrophilic substitution due to the nucleophilic central carbon atom forming 3-substituted acac derivatives. Besides their significant role in coordination chemistry, they are key precursors in rapidly developing fields such as nanoparticle research, polymer science, and catalysis (both homo- and heterogeneous) [54].

In hydroxyflavone-based metal complexes exhibiting a 4-carbonyl/5-hydroxyl coordination mode, the ligand acts as a bidentate chelator, coordinating the metal center through two oxygen atoms located on adjacent aromatic rings, namely the carbonyl group at position C-4 on the C-ring and the hydroxyl group at position C-5 on the A-ring. This (O,O)-coordination mode results in the formation of a six-membered chelate ring.

The spectroscopic features associated with this coordination pattern largely mirror those observed in maltol-type (3-hydroxy-4-keto) complexes. However, the key distinction lies in the ^{1}H NMR spectrum, where the characteristic signal of the C-5 hydroxyl proton disappears, providing direct evidence of its involvement in metal coordination. In contrast to 3-OH–F complexes, where coordination primarily involves the C-ring and affects band I, the 4-carbonyl/5-hydroxyl coordination mode may also induce minor spectral shifts in band II, associated with electronic transitions in the A-ring. This subtle bathochromic or hypsochromic shift further supports the involvement of the A-ring 5-hydroxyl group in metal coordination.

The series of Co(III) complexes **56**–**68** synthesized by Kozsup et al. (Table 11), previously reviewed in Section 2.1, has been expanded with two additional complexes, **69** and **70** (Figure 13) featuring a chrysin moiety capable of acac-type coordination (Table 13) [45]. The coordination chemistry is well established, as seen in their maltol-type analogs, and is supported by NMR, IR, and HRMS characterization data. The crystal structure analysis of complex **69** confirmed the proposed coordination mode. While chrysin, the metal precursors, and **69** exhibited no cytotoxicity against A431 and A549 cell lines, complex **70**, obtained with [Co(tpa)Cl_2]Cl, demonstrated improved activity in both cell lines under the

tested conditions. A previously spotted trend for more active compounds with tpa moiety was confirmed for acac complexes **69** and **70** as well.

Table 13. Numeration of Co(III) complexes **69** and **70** obtained by acac-type coordination and their cytotoxicity against A431 and A549 human cancer cell lines under normoxic and hypoxic conditions after 72 h incubation using end-point SRB assay. EC_{50} and 95% confidence interval (CI) values are presented in μM as a mean of three independent experiments [53].

Compd.	Abbr.	EC_{50}(μM)			
		A431		A549	
		Normoxia	Hypoxia	Normoxia	Hypoxia
chrysH	–	>100	>100	>100	>100
[Co(tren)Cl_2]Cl	–	>100	>100	>100	>100
[Co(tpa)Cl_2]Cl	–	>100	>100	>100	>100
[Co(tren)(chrys)](Cl)(ClO_4)	**69**	>100	>100	>100	>100
[Co(tpa)(chrys)](ClO_4)$_2$	**70**	68 [+17, −13]	64 [+15, −12]	34 [+4, −3]	33 [+5, −4]
cisplatin	–	3.2 [+0.7, −0.6]	5.6 [+1.3, −1.1]	1.8 [+0.2, −0.2]	2.4 [+0.7, −0.6]

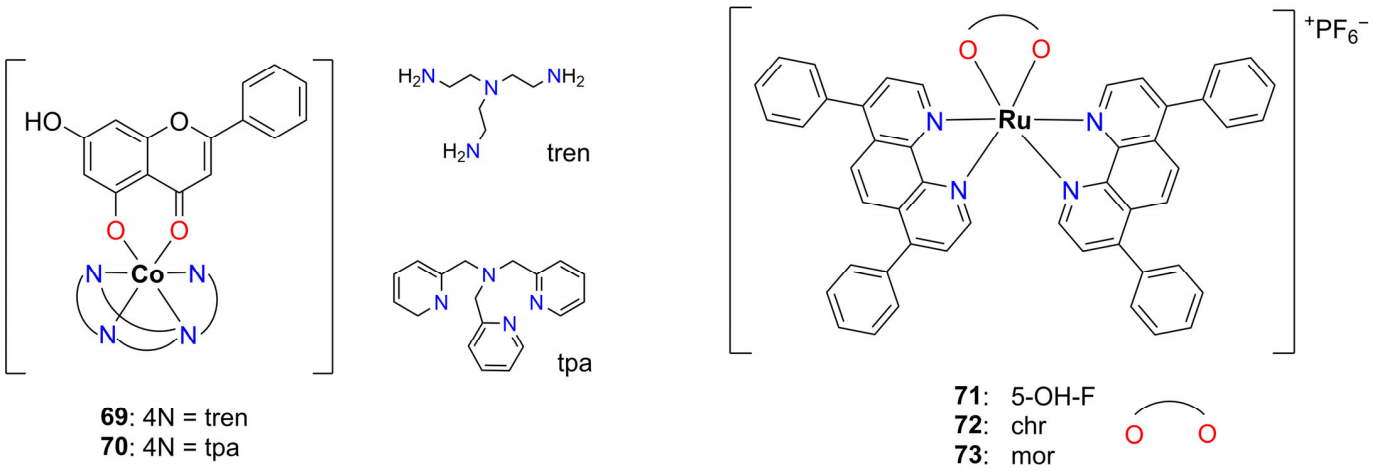


Figure 13. The chemical structures of Co(III) complexes **69** and **70**, as reported by Kozsup et al. [53], and Ru(II) representatives (**71**–**73**), as reported by Gasser's group [55].

In the same year, the research group of Gasser published a series of monocationic Ru(II) polypyridyl complexes **71**–**73** of the type [Ru(DIP)$_2$(OH–F)]X (Figure 13), containing 4,7-diphenyl-1,10-phenanthroline (DIP), OH–F (5-hydroxyflavone, chrysin, or morin) and X as the counterion, PF_6^-, and OTf^- [55]. These complexes were obtained by different synthetic routes which can be summarized as the following: all complexes were obtained starting from the metal precursor, Ru(DIP)$_2$Cl$_2$, in EtOH under N_2 and protected from light. Compound **71**, [Ru(DIP)$_2$(5-OHF)](PF_6), carrying 5-hydroxyflavone, involved direct coordination in the presence of NaOH. For the rest of the two complexes with chrysin (**72**, [Ru(DIP)$_2$(chr)](PF_6)), or morin (**73**, [Ru(DIP)$_2$(mor)](PF_6)), respectively, silver triflate was used prior to the addition of ligands. In the case of morin-based complex **73**, the ligand was silylated with tetramethylsilane (TMS) bromide in THF before complexation, though it later appeared to be unnecessary as TMS protecting groups were hydrolyzed during the complexation. The reactions for all compounds **71**–**73** involved refluxing (1.5–2 h), followed by cooling, solvent removal under a vacuum, and purification via DCM extraction, NH_4PF_6 precipitation, or Celite filtration, and preparative thin-layer chromatography (TLC) as needed. The final isolation steps included sequential washes with Et_2O and heptane,

sonication, centrifugation, and vacuum drying to obtain the purified Ru(II) complexes in a form of a racemic mixture of Δ and Λ enantiomers. The chemical characterization included HRMS and NMR spectroscopy while their purity was checked using EA. Prior to the cytotoxicity study, the stability of **71**–**73** was confirmed by NMR in DMSO for 5 days.

The biological profile of Ru(II) complexes **71**–**73** was evaluated using a fluorometric cell viability assay on four human cancer cell lines MCF-7 (breast), hypopharyngeal squamous cell carcinoma (FaDU), metastatic breast cancer cell line (MDA-MB-435S), and U87 (glioblastoma), as well as on two non-cancerous cell lines, RPE-1 (retina) and embryonic kidney (HEK293) cells. Cisplatin and doxorubicin were used as positive controls (Table 14). Among the complexes' precursors, only chrysin was found to be active mainly against HEK293 (IC_{50} = 26.80 ± 2.79), while $[Ru(DIP)_2]Cl_2$ showed good activity on the RPE-1 cell line with IC_{50} = 3.13 ± 0.28. However, the coordination via Ru(II) significantly improved starting IC_{50} values for the majority of **71**–**73** complexes. None of the complexes **71**–**73** showed activity against the MCF-7 cell line. While they exhibited some activity against other tested cell lines, no selectivity for cancerous over normal cell lines was observed.

Table 14. Cytotoxicity results for reviewed Ru(II) **71**–**73** complexes obtained by acac-type coordination and their precursors after 48 h treatment using the fluorometric cell viability assay on tested human cell lines [55].

Compd.	IC_{50} (μM)					
	MCF-7	**FaDU**	**MDA-MB-435S**	**U87**	**RPE-1**	**HEK293**
5-OH–F	>100	>100	>100	>100	>100	>100
chr	62.59 ± 3.23	95.06 ± 11.55	79.37 ± 8.13	91.14 ± 13.76	>100	26.80 ± 2.79
mor	>100	>100	>100	>100	>100	>100
CDDP	19.69 ± 1.63	5.17 ± 0.21	17.62 ± 0.54	6.94 ± 0.46	39.9 ± 9.14	2.27 ± 0.67
Dox. *	9.39 ± 1.37	1.55 ± 0.18	5.55 ± 1.37	0.59 ± 0.03	14.90 ± 1.31	0.21 ± 0.03
prec. *	>50	>50	27.73 ± 5.33	25.59 ± 0.29	3.13 ± 0.28	12.11 ± 1.30
71	>50	38.21 ± 5.22	24.48 ± 1.92	30.72 ± 1.48	19.72 ± 8.23	24.46 ± 3.20
72	>50	>50	27.73 ± 5.33	25.59 ± 0.29	23.21 ± 8.08	33.02 ± 3.25
73	>50	>50	>50	>50	>50	>50

* Dox. doxorubicin; prec. precursor $[Ru(DIP)_2Cl_2]$.

Munteanu et al. studied four mononuclear lanthanide-containing complexes, **74**–**77**, with 5-hydroxyflavone and phen (Figure 14) [56]. A series of complexes containing Ln(III) metal ions were synthesized by reacting the corresponding metal chlorides, $LnCl_3$, with deprotonated 5-OH–F in the presence of triethylamine and an ethanolic solution of phen. The reactions were carried out under reflux, yielding yellow products with the general formula $[Ln(OH)_2(5\text{-OH–F})(phen)]\cdot nH_2O$, where n = 4, 3.5, 2, and 3 for Sm(III), Eu(III), Gd(III), and Tb(III), respectively. The physicochemical characterization of newly synthesized compounds included UV–Vis, IR, HRMS, EA, and TA. According to a DFT study, authors suggested a six-coordinated distorted octahedron geometry for all four complexes. The next step included the evaluation of the cytotoxic effects for both ligands and complexes on five human cancer cell lines (HeLa (cervix), colorectal adenocarcinoma (HT-29), colon adenocarcinoma (LoVo), MCF-7 (breast), and ovarian adenocarcinoma (SK-OV-3)) using cisplatin and doxorubicin as positive controls. Cell viability tests were performed by MTS assay within the incubation period of 48 h. Interestingly, obtained IC_{50} values indicated a relatively good cytotoxic activity for reported complexes, **74**–**77**, particularly against MCF-7 cancer cells (Table 15). In this case, IC_{50} values for **74**–**77** were remarkably close to doxorubicin, highlighting the Eu(III)-complex **75** as the most active one. Regarding the cytotoxic profile of the precursor compounds, 5-HO–F showed an enhanced cytotoxicity in HeLa cells in comparison to Ln(III) complexes, while the Sm(III)-complex **74** demonstrated

a lower IC_{50} in comparison to cisplatin (13.78 vs. 31.55 μM). In parallel, 5-HO–F was not active on HT-29 cells in contrast to **74**–**77** which were more potent than cisplatin. Moreover, in the cases of LoVo and SK-OV-3, the investigated complexes **74**–**77** displayed better activity in comparison to free ligands and cisplatin, especially against LoVo. Therefore, the authors chose HeLa and LoVo cell lines to proceed with the biological profiling that involved apoptotic effects, DNA-binding, and serum-protein-binding studies.

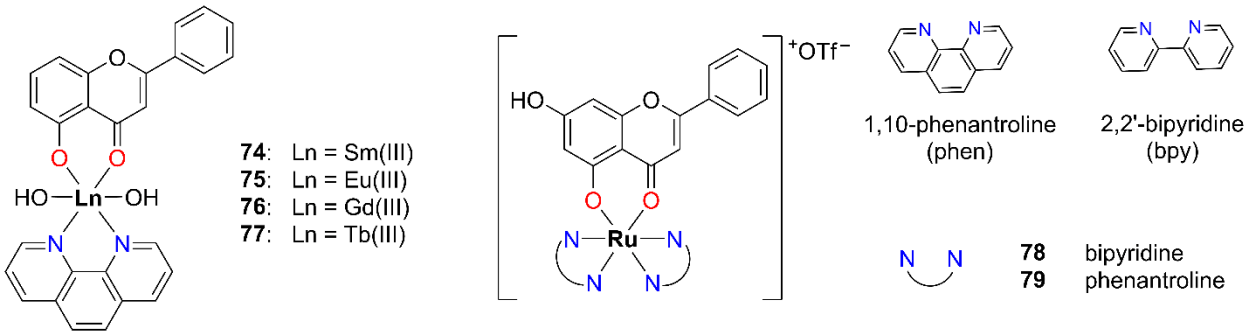


Figure 14. The proposed structures of Ln(III) complexes **74**–**77**, as reported by Munteanu et al. [56], and Ru(II) complexes **78**–**79**, as reported by Zahirović et al. [50].

Table 15. Cytotoxicity results for reviewed $[Ln^{III}(OH)_2(5\text{-OH–F})(phen)]\cdot nH_2O$ complexes **74**–**77** obtained by acac-type coordination and their precursors after 48 h treatment using MTS assay on five cancer human cell lines: HeLa, HT-29, LoVo, MCF-7, and SK-OV-3 [56].

Compd.	Ln(III)	IC_{50} (μM)				
		HeLa	HT-29	LoVo	MCF-7	SK-OV-3
5-HO–F	–	5.94 ± 1.77	118.81 ± 16.93	33.67 ± 6.46	30.43 ± 5.85	60.27 ± 5.03
phen	–	50.99 ± 6.51	7.81 ± 1.89	33.86 ± 5.15	7.59 ± 3.25	60.11 ± 7.97
74	**Sm**	13.78 ±1.51	24.71 ± 4.52	8.22 ± 2.01	7.62 ± 3.68	36.28 ± 3.73
75	**Eu**	36.55 ± 3.30	17.24 ± 2.41	11.32 ± 2.44	2.50 ± 2.18	43.44 ± 3.69
76	**Gd**	31.75 ± 2.74	35.18 ± 6.44	17.63 ± 3.84	3.35 ± 0.61	41.03 ± 3.99
77	**Tb**	31.55 ± 2.76	20.47 ± 2.75	27.55 ± 3.84	3.60 ± 0.46	31.13 ± 2.93
cisplatin	–	24.06 ± 2.51	53.62 ± 4.68	30.47 ± 5.36	n.e.	50.85 ± 4.32
doxorubicin	–	n.e.	n.e.	n.e.	3.27 ± 0.45	n.e.

n.e.—not evaluated

Moreover, all synthesized complexes demonstrated potential as DNA intercalators. This claim was supported by UV–Vis spectroscopy and various fluorescence-based assays (EB displacement assay, SYBR Gold® fluorescence quenching assay, and Alexa488 fluorescence quenching assay) and viscosimetric studies. These findings provided insights into binding dynamics, confirming effective DNA binding at micromolar concentrations highlighting the Sm(III)-complex **74** as the compound with the fastest binding kinetics and the highest activity. Molecular docking simulations further supported the intercalative binding mode. In addition to DNA interaction, the lanthanide complexes displayed effective binding to serum transport proteins, with a generally higher affinity for human serum albumin (HSA) compared to transferrin (Tf). Importantly, the authors underlined the significant role of structural flexibility in macromolecular interactions, as binding to DNA or proteins was accompanied by distinct conformational rearrangements. Overall, this study introduces four novel Ln(III) complexes capable of targeting multiple cellular components indicating how the integration of multiple (hetero)cyclic motifs and the adaptable coordination environment of trivalent lanthanide ions present a promising platform for the development of multimodal anticancer agents.

As previously discussed in the section on maltol-type coordination, Zahirović et al. synthesized mixed-ligand complexes with Ru(II) [50]. This time, complexes **78** and **79,** incorporating the hydroxyflavone chrysin, which lacks a 3-hydroxyl group, formed six-membered chelate rings (Figure 14).

Cytotoxicity was evaluated using the MTT assay after 72 h of treatment, and the results are presented in Table 16. Complex **78**, containing bpy, exhibited the best activity against the MCF-7 cell line, while complex **79**, bearing phen, showed the highest cytotoxicity toward the HeLa cell line.

Table 16. Cytotoxicity of complexes **78**–**79** determined by MTT assay after 72 h treatment expressed as (mean ± SD, n = 3) [50].

Compd.	IC_{50} (μM)			
	SW620	**HepG-2**	**MCF-7**	**HeLa**
chrysin	43.01 ± 16.34	85.81 ± 51.93	63.81 ± 25.45	33.82 ± 9.95
***cis*-[Ru(bpy)$_2$Cl$_2$]·2H$_2$O**	>100	4.53 ± 60.11	2.10 ± 70.64	>100
[Ru(phen)$_2$(CO$_3$)]·2H$_2$O	>100	>100	92.38 ± 44.00	>100
78	62.78 ± 19.36	45.02 ± 6.67	12.55 ± 18.18	26.80 ± 1.21
79	53.39 ± 36.52	43.26 ± 21.31	43.67 ± 37.06	8.42 ± 20.23

The antimicrobial activity of complex **78** is approximately two to three times lower than that of standard antibiotics, except in the case of MRSA, where its efficacy is comparable to that of gentamicin (Table 17). Compound **79** exhibits roughly half the antibacterial activity of gentamicin against *Acinetobacter baumannii* ATCC BAA-747, yet demonstrates slightly higher activity than the parent flavonoid, chrysin.

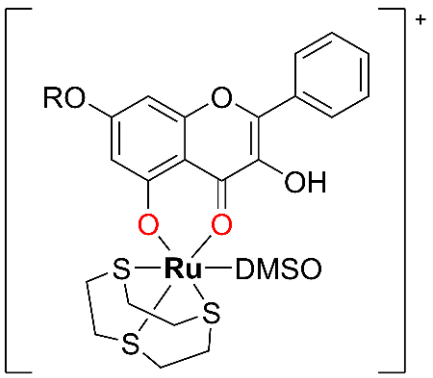
Table 17. Antimicrobial activity of free chrysin and its ruthenium (II) complexes [Ru(bpy/phen)$_2$(chrys)](OTf)·nH$_2$O, evaluated using the disk diffusion method and expressed as inhibition zone diameters (mm) [50].

Compd.	*Staphylococcus aureus* ATCC 25923	*Enterococcus faecalis* ATCC 19433	*Streptococcus* Beta-Hemolytic Group A	Methicillin-Resistant *Staphylococcus aureus*	*Klebsiella pneumoniae* ATCC 1705	*Acinetobacter baumannii* ATCC—BAA 747	*Pseudomonas aeruginosa*	*Escherichia coli*	*Candida albicans*
	G+	G+	G+	G+	G−	G−	G−	G−	Fungus
	Diameter of Inhibition Zone (mm)								
chrysin	*	*	*	*	*	14	*	*	14
***cis*-[Ru(bpy)$_2$Cl$_2$]**	*	*	*	*	*	15	*	*	14
[Ru(phen)$_2$CO$_3$]	*	*	*	*	*	15	11	*	15
78	15	*	15	16	*	13	*	*	17
79	*	*	*	*	*	17	*	*	*
vancomycin	27	26	35	-	-	-	-	-	-
gentamicin	-	-	-	20	25	35	36	21	-
nystatin	-	-	-	-	-	-	-	-	28

* No activity, - not tested, G+ = Gram-positive bacteria, and G− = Gram-negative bacterial strain.

In 2019, Marques et al. contributed to the field of Ru(II) metal complexes with OH–F motifs coordinated in acac mode by reporting two Ru(II) trithiacyclononane ([9]aneS$_3$) complexes, **80**–**81,** presented in Figure 15 [57]. Ru(II) complex **80** was synthesized by reacting chrysin with one equivalent of [Ru(II)([9]aneS$_3$)Cl$_2$(S-DMSO)] and half an equivalent of tetrabutylammonium hydroxide. The light yellow solution was refluxed in methanol for 24 h. Upon evaporation to half its volume, the mixture yielded both complex **80** and an unreacted metal precursor. The pure form of **80** was obtained by filtration of the supernatant, followed by volumization with an additional portion of diethyl ether. After one week at 4 °C, complex **80** ([Ru(II)([9]aneS$_3$)(chrys)(*S*-DMSO)]Cl) was isolated as a dark orange solid, washed with cold ethanol and diethyl ether, and dried. Prior to the synthesis of the

second complex (**81**), the ligand precursor 5-hydroxy-7-methoxyflavone (tectochrysin, tchr) was prepared by reacting chrysin with potassium carbonate (1:3 molar ratio), followed by the addition of dimethyl sulfate. The reaction mixture was refluxed in acetone for one hour, yielding a yellow precipitate that was purified via column chromatography and recrystallization from a dichloromethane/methanol mixture. In the following synthetic step, complex **81**, also featuring acac-type coordination, was synthesized by reacting tchr with [Ru(II)([9]aneS_3)Cl_2(S-DMSO)] in a 1:1 molar ratio under a 24 h reflux in methanol, with the addition of tetrabutylammonium hydroxide. After cooling, diethyl ether and dichloromethane were added to isolate the dark orange oily product. To obtain a solid form of **81**, several recrystallization steps were performed in dichloromethane, followed by washing with diethyl ether. Unlike complex **80**, which was obtained in relatively low yields (23%, respectively), **2** was synthesized in a slightly improved yield of 43%. Both compounds (**80** and **81**) were characterized by IR, ^{1}H, and ^{13}C NMR spectroscopy, HRMS, and EA.



80: R = H
81: R = CH_3

Figure 15. The proposed chemical structures of Ru(II) trythiacyclononane complexes **80**–**81**, featuring acac-type coordination, as reported by Marques et al. [57].

The cytotoxic effects of Ru(II) trithiacyclononane ([9]aneS_3) complexes **80**–**81** and their precursor compounds (chr and tchr) were evaluated against three cancer types using four human cancer cell lines: osteosarcoma cell line (MG-63), PC-3 (prostate), MCF-7 (breast), and MDA-MB-231 (breast) (Table 18). Cell viability was assessed using the MTT assay after a 72 h incubation period, with cisplatin as a positive control. Interestingly, the pure ligands exhibited stronger cytotoxicity, particularly against osteosarcoma cells, with the 5-methoxy derivative of chr showing the most promising effect. This finding is especially valuable given the limited availability of effective chemotherapeutic options for osteosarcoma. Moreover, OH–F compounds are generally associated with milder side effects, adding further therapeutic relevance to these results. Simultaneously, complexes **80** and **81** displayed mild cytotoxic activity, which is rather modest compared to the numerous previous studies reporting enhanced bioactivity upon metal complexation [58].

Table 18. The cytotoxicty of reviewed Ru(II) complexes **80**–**81** obtained by acac-type coordination against MG-63, PC-3, MCF-7, and MDA-MB-231 after 72 h of incubation using MTT assay and cisplatin as a positive control [57].

Compd.	IC_{50} (μM)			
	MG-63	PC-3	MCF-7	MDA-MB-231
chr	41.0	15.7	29.5	17.1
80	>200 [a]	146.2	>200 [a]	180.6
tchr	67.9	32.8	113.5	44.8
81	>200 [a]	>200 [a]	>200 [a]	>200 [a]
cisplatin	4.5	6.6	13.8	9.5

[a] Growth inhibition at 200 μM, the highest concentration tested, was lower than 50%.

2.3. Catechol-Type Coordination

Wherever two vicinal hydroxyl groups are present within the OH–F molecule, catechol-type coordination to a metal center may occur, leading to the formation of a five-membered chelate ring. Upon coordination, the deprotonation of the hydroxyl groups is expected, which can be observed as the disappearance of the corresponding signals in the ^{1}H NMR spectrum, along with characteristic changes in the UV–Vis spectrum.

A representative example of catechol-type coordination is described in the work of Naso et al., which reports an oxidovanadium(IV) complex with luteolin, $[VO(lut)(H_2O)_2]Na{\cdot}3H_2O$ (compound **82**; Figure 16) [59]. The background behind designing such a complex originates from both the favorable biological profile of luteolin, known for its antioxidant, anti-inflammatory, antimicrobial, and anticancer activities [60], and the well-documented therapeutic potential of oxidovanadium(IV) complexes with other flavonoids [61–63]. Complex **82** was synthesized by reacting $VOCl_2$ with luteolin in a 1:2 molar ratio in ethanol, with the pH of the reaction mixture adjusted to five using 1 M NaOH. After 3 h of reflux, a dark green precipitate formed, which was isolated by filtration, washed with ethanol, and dried to yield the pure compound. The proposed structure of **82** was based on EA, UV–Vis spectroscopy, and TGA. Electron paramagnetic resonance (EPR) spectroscopy revealed the presence of two coordinated water molecules and two phenolate (ArO^-) groups in the metal's coordination sphere. Moreover, EPR data indicated the formation of chains involving adjacent VO units, as supported by calculated exchange pathways. Prior to biological evaluation, the stability of **82** was confirmed by monitoring its electronic absorption spectra in DMSO under N_2 atmosphere, which remained unchanged over time, indicating good solution stability.

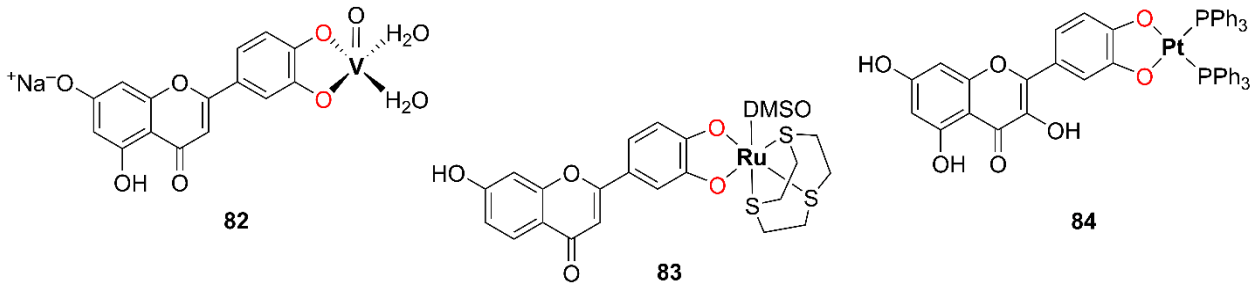


Figure 16. The proposed chemical structures of catechol-type coordinated hydroxyflavones: oxidovanadium(IV) complex **82** with luteolin, as reported by Naso et al. [59], and Ru(II) complex **83** with 7,3′,4′-OH–Fand trythiacyclononane, as reported by Marques et al. [57], and Pt(II)complex **84** with quercetin and triphenylphosphine (PPh_3), as reported by Dell'Anna et al. [37].

Cell viability assays were conducted using the crystal violet assay for A549 (lung) cells and the MTT assay for MDA-MB-231 (breast) cells (Table 19). For the A549 cell line, cells

were incubated at 37 °C in a growth medium for 24 h, after which the medium was replaced with fresh solutions of luteolin and complex **82**. Following additional 24 h incubation, cells were stained with crystal violet. The cytotoxicity evaluation revealed comparable IC_{50} values for both compounds, 66.3 μM for luteolin, and 60.5 μM for complex **82**. It is worth noting that significantly lower IC_{50} values have been reported in other studies [64].

Table 19. Studied oxidovanadium(IV) complex **82** obtained by catechol-type coordination and its cytotoxicity against two cell lines (A549 using crystal violet assay and MDA-MB-231 using MTT assay) [59].

Compd.	IC_{50} (μM)	
	A549	**MDA-MB-231**
luteolin	66.3	88.3
82	60.5	17.0

In the next step, the MTT assay was applied to MDA-MB-231 cells treated with varying concentrations (0–100 μM) of luteolin and complex **82**. After 24 h of incubation, luteolin exhibited an IC_{50} value of 88.3 μM, consistent with previously reported data. In contrast, its oxidovanadium(IV) complex, **82**, demonstrated significantly enhanced cytotoxicity, with an IC_{50} of 17.0 μM. According to the authors of this study, the obtained results underscore the role of metal coordination in enhancing the anticancer activity of luteolin, as previously reported for vanadium complexes [65].

In addition to inducing cellular reactive oxygen species (ROS) generation and mitotic arrest, both luteolin and its oxidovanadium(IV) complex (VOlut) cause damage to the cytoplasmic and nuclear membranes. Their binding to bovine serum albumin (BSA) involves a combined quenching mechanism, with static quenching being the dominant process. Thermodynamic parameters, derived from the Van't Hoff equation, revealed that the interactions are spontaneous. The luteolin–BSA complex is primarily stabilized by electrostatic forces, whereas the VOlut–BSA interaction is mainly driven by hydrogen bonding and van der Waals forces. Given the confirmed cytotoxic effects of both luteolin and **82**, the complex shows potential as a promising candidate for further in vivo evaluations in cancer treatment studies.

Beside two acac-type coordinated complexes, Marques et al. (reference [57] in previous Section) prepared a catechol-type Ru(II) complex **83** (Figure 16). It was synthesized by reacting 7,3′,4′-OH–F with the metal precursor [Ru([9]aneS_3)Cl_2(DMSO)] in a 1:1 molar ratio, in the presence of one equivalent of tetrabutylammonium hydroxide in ethanol. The reaction mixture was refluxed for 48 h, during which the solution changed color from light yellow to orange and finally to the dark green solid product. Complex **83** was isolated by washing with ethanol and diethyl ether, then dried. According to the cytotoxicity test, complex **83** was inactive, likely due to its limited water solubility (Table 20).

Table 20. The cytotoxicty of reviewed Ru(II) complex obtained by catechol-type coordination against MG-63, PC-3, MCF-7, and MDA-MB-231 after 72 h of incubation using MTT assay and cisplatin as a positive control [57].

Compd.	IC_{50} (μM)			
	MG-63	**PC-3**	**MCF-7**	**MDA-MB-231**
7,3′,4′-OH–F	38.1	23.2	36.9	24.8
83	>18.5 [a]	>18.5 [a]	>18.5 [a]	>18.5 [a]
cisplatin	4.5	6.6	13.8	9.5

[a] An amount of 18.5 was the highest concentration tested for **84** due to its low solubility.

As previously mentioned in Section 2.1, Dell'Anna et al. [37] synthesized Pt(II) complexes with OH–F and PPh_3. One of the complexes (**84**), shown in Figure 16, features quercetin coordinated in a catechol-type fashion. The complex was synthesized using the same procedure as described for the maltol-type complex, with the exception that the precipitate was obtained using *n*-hexane instead of *n*-pentane. In this case, slow diffusion of *n*-pentane into a THF solution containing the respective complex over a period of two weeks yielded crystals suitable for XRD analysis. The complex crystallizes in the orthorhombic crystal system. Probably due to the multiple possible coordination modes of quercetin, complex **84** was obtained with approximately 5% impurities, which the authors were unable to separate. Consequently, the cytotoxicity of the complex was not evaluated.

2.4. Mixed-Type Coordination

The combination of both acac- and catechol-type coordination modes within the same complex molecule can lead to so-called mixed coordination. The observed spectral changes will reflect a combination of features characteristic of both acac- and catechol-type coordinated complexes.

One of the earliest examples of mixed-type coordination was reported by Ikeda et al., who described the synthesis and characterization of a rutin–zinc (II) flavonoid–metal complex (Figure 17) [35]. The rutin–Zn(II) complex **85** was synthesized by the slow addition of an aqueous solution of $[Zn(CH_3COO)_2]\cdot 2H_2O$ to a methanolic solution of dehydrated rutin. The reaction mixture was stirred at temperatures up to 40 °C for 24 h, after which the resulting complex **85** was isolated by filtration, rinsed with methanol, and dried. Structural characterization of compound **85** was carried out using IR spectroscopy, ^{1}H NMR, UV–Vis spectroscopy, and EA. The proposed structure (Figure 17) features a mixed coordination mode, involving both catechol-type coordination via the 3′,4′-dihydroxy groups of the B-ring and acac-type coordination via the 4-keto and 5-hydroxy groups of the C-ring.

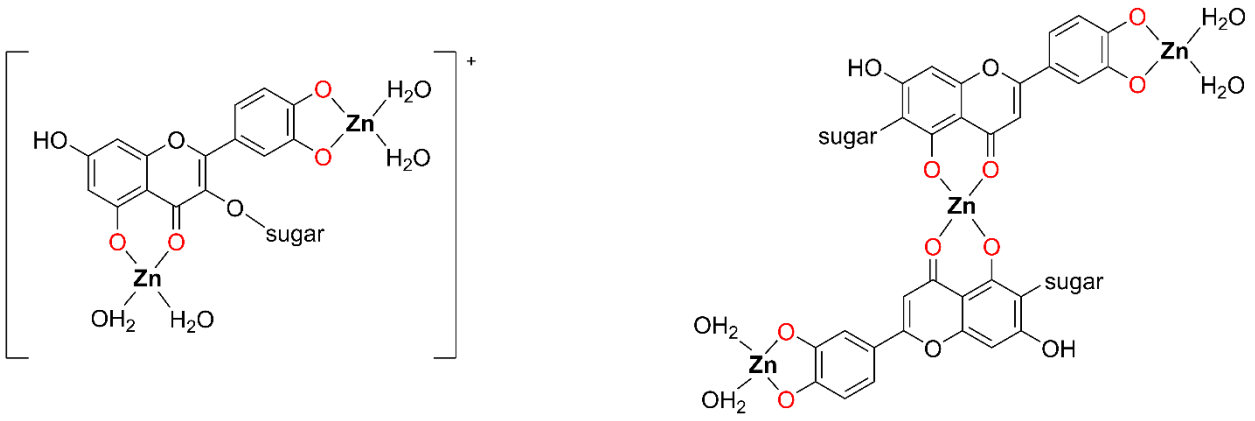


Figure 17. The proposed chemical structures of Zn(II) complexes with mixed-type coordination mode: the cationic complex **85** with rutin, reported by Ikeda et al. [35], and the neutral complex **86** with isoorientin, reported by Wang et al. [36].

This dual chelation stabilizes the complex and is typical of flavonoid–metal interactions.

The cytotoxicity study was conducted on a panel of cancer cell lines, including murine melanoma (B16F10, derived from a C57BL/6J mouse), human skin melanoma (SK-MEL-28), acute myelogenous leukemia (KG-1), multiple myeloma (RPMI 8226), T-cell leukemia (Jurkat), and chronic myelogenous leukemia (K562), as well as on normal human cell lines, namely fibroblasts and umbilical vein endothelial cells (HUVECs). Cells were treated with compound **85** and its precursor rutin over a concentration range of 17.2–275.6 μM for 24 h.

Cell viability was then assessed using the MTT assay (Table 21). While rutin alone exhibited no cytotoxic effects on either cancerous or healthy cells, and was therefore not included in the IC_{50} analysis, compound **85** showed significant cytotoxic activity against all tested tumor cell lines.

Table 21. Studied Zn(II) complex **85** obtained by mixed-type coordination and its cytotoxicity assessed by MTT assay against eight cell lines after 24 h incubation [35].

Cell Line	IC_{50} (μM)
B16F10	160.7
SK-MEL-28	194.0
KG-1	91.4
RPMI 8226	196.6
Jurkat	150.2
K562	173.2
Fibroblasts	>275.6
HUVEC	>275.6

Importantly, **85** displayed favorable selectivity, as no cytotoxic effect was observed on normal (non-cancerous) cells. Although the compound demonstrated its strongest anticancer activity against the KG-1 leukemia cell line, it is worth noting that the study did not include a comparison with a standard positive control, which limits the interpretation of its relative potency.

In addition, Ikeda et al. reported in vivo toxicological studies in female mice. Both rutin and **85** were administered intraperitoneally (i.p.) for 7, 14 and 21 days. The toxicity was observed for 30, 60, and 90 days after the initial treatment following the parameters such as body weight measurement, hematological and biochemical analyses, and histological examination of the liver and kidneys. After 21 days of treatment, mice treated with rutin and **85** showed increased platelet, red blood cell, and white blood cell counts, which returned to normal after 90 days. A histopathological analysis revealed no abnormalities in the liver, kidneys, or lungs compared to controls. Mitochondrial membrane potential (Δψm) was evaluated by flow cytometry using Rhodamine 123. Significant loss of Δψm was observed in Ehrlich ascites carcinoma (EAC) cells treated with paclitaxel or its combinations with rutin and Rutin–zinc (II), although the single compounds had milder effects.

In vivo studies in EAC-bearing mice showed that **85** induced stronger DNA fragmentation in tumor cells than rutin alone. When combined with paclitaxel, both compounds significantly enhanced DNA fragmentation. These effects were associated with the activation of caspase-dependent apoptosis, reduced cyclin D1 and vascular endothelial growth factor (VEGF) expression, and upregulation of caspases-8 and -3. Importantly, the combination of the Rutin–zinc (II) complex, **85**, with paclitaxel exhibited synergistic antitumor activity, reduced anemia and myelosuppression, common side effects of chemotherapy, and increased the survival of tumor-bearing mice.

In one of their recent studies, Wang et al. synthesized and characterized a trinuclear Zn(II) complex **86** (Figure 17) using OH–F isoorientin (iso) as a ligand [36]. This natural bioactive flavonoid C-glycoside was selected due to its broad biological activity, including anticancer and antioxidant properties [66], as well as antibacterial activity [67]. The complex was synthesized by reacting the iso ligand in ethanol with $Zn(CH_3COO)_2 \cdot 2H_2O$. After adjusting the pH to approximately eight, the reaction mixture was stirred and refluxed for 8 h. Upon cooling, a brown-yellow precipitate formed, which was isolated, washed with ethanol, dried, and stored at 4 °C. Comprehensive characterization of the complex was performed using ^1H NMR and IR spectroscopy, EA, and TGA. To further support the

proposed structure, UV–Vis spectroscopy, inductively coupled plasma atomic emission spectrometry (ICP-AES), and SEM were also employed.

The biological profiling of **86** was initiated with antibacterial activity assays, which included measurements of the bacteriostatic zone diameter, bacteriostatic rate, and bacterial growth curves. Antibacterial effects were evaluated against *Escherichia coli* and *Staphylococcus aureus* using the disk diffusion method. Initial results revealed stronger antibacterial effects of both **86** and its precursor iso against *S. aureus* compared to *E. coli*, across the same concentration range (0, 200, 400, 600, and 800 μg/mL, Table 22). Notably, **86** exhibited higher bacteriostatic rates against both bacterial strains compared to the free ligand. Additionally, a concentration-dependent increase in the diameter of the bacteriostatic zone was observed for both compounds, with **86** consistently outperforming iso (Table 23). These findings suggest that coordination with Zn(II) enhances the antibacterial efficacy of isoorientin, resulting in a stronger bacteriostatic effect. The next phase of the antibacterial study assessed the effects of iso and **86** on bacterial cell membrane integrity using SEM and transmission electron microscopy (TEM) techniques. Morphological and ultrastructural analyses revealed visible alterations in cell shape and clear signs of membrane damage, primarily induced by compound **86** and, to a lesser extent, iso. The main indication of this membrane disruption was the leakage of cytoplasmic contents, accompanied by an increase in electrical conductivity in the surrounding medium. This effect was attributed to the release of proteins and nucleic acids, as well as the continuous efflux of intracellular electrolytes such as K^+ and Na^+ ions. The observed damage was more pronounced in cells treated with complex **86**, suggesting its superior antibacterial efficacy. This enhancement is likely due to structural and property changes upon Zn(II) coordination, which may increase the compound's ability to interact with bacterial proteins and DNA. Finally, the authors suggested the influence of a synergistic effect, meaning that the combination of the ligand (iso) and the metal (**Zn**) works better than either component alone.

Table 22. Summarized inhibition zone diameters and inhibition rates of isoorientin (iso) and complex **86** on *E. coli* and *S. aureus* [36].

Compd.	Concentration (μg/mL)	*E. coli*		*S. aureus*	
		Diameter of Bacteriostatic Circle (mm)	Bacteriostatic Rate (%)	Diameter of Bacteriostatic Circle (mm)	Bacteriostatic Rate (%)
iso	0	6.03 ± 0.23	0.00	6.06 ± 0.12	0.00
	200	6.08 ± 0.15	0.82	8.29 ± 0.31	26.90
	400	8.10 ± 0.24	25.56	10.83 ± 0.29	44.04
	600	11.13 ± 0.27	45.82	12.62 ± 0.14	51.98
	800	13.29 ± 0.25	54.62	14.16 ± 0.35	57.20
86	0	6.04 ± 0.28	0.00	6.07 ± 0.17	0.00
	200	7.69 ± 0.16	21.46	10.66 ± 0.32	43.06
	400	9.46 ± 0.18	36.62	12.24 ± 0.27	50.41
	600	11.97 ± 0.39	49.54	13.91 ± 0.36	56.36
	800	15.37 ± 0.44	60.70	16.59 ± 0.21	63.41

The cytotoxicity evaluation included both a hemolysis assay and an MTT assay for cell viability. The hemolysis assay was performed following the protocol described by Liu et al. in 2009 [68], using a microplate reader for absorbance measurements. The results provided clear evidence that both **86** and iso inhibited erythrocyte hemolysis. As lipid peroxidation of the erythrocyte membrane is typically induced by hydrogen peroxide (H_2O_2), the authors observed that **86** exhibited low cytotoxicity even after H_2O_2 exposure, indicating its favorable safety profile for potential therapeutic applications. This observation was further

supported in the final stage of **86** biological profiling, which involved assessing cell viability using the MTT assay, following a slightly modified protocol based on Yuan et al. [69]. The experiments were conducted on normal human liver cells (HL-7702) and the results showed no significant difference in viability between the **86**-treated group and the untreated control, indicating low cytotoxicity toward normal hepatocytes. Overall, the findings of this study classify the **86**-type of compounds as primarily antibacterial agents rather than for anticancer compounds.

Table 23. MIC values of studied compounds iso and **86** against *E. coli* and *S. aureus* [36].

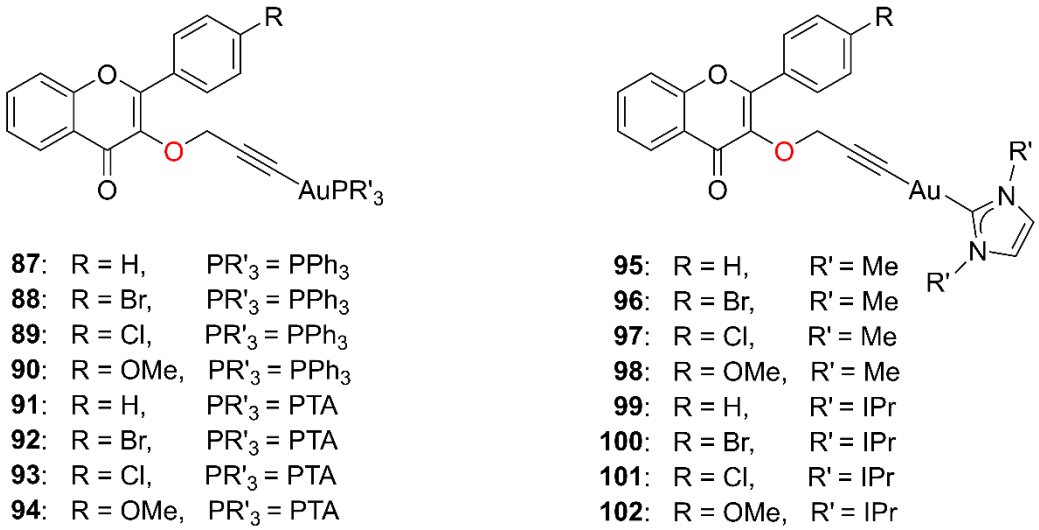
Compd.	Bacteria	Concentration (μg/mL)					
		0	50	100	200	400	800
iso	*E. coli*	++	++	+	+	-	-
	S. aureus	++	+	+	-	-	-
86	*E. coli*	++	++	+	-	-	-
	S. aureus	++	+	-	-	-	-

+ Indicates small amount of bacterial growth. ++ Indicates mass bacterial growth. - Indicates no bacterial growth.

2.5. Linear-Type Coordination

A characteristic feature of this type of complex is coordination through a single hydroxyl group of the OH–F ligand.

In 2019, Mármol et al. described the synthesis and a full characterization of flavone-based ligands bearing propargyl ether group and their corresponding phosphane gold(I) complexes (Figure 18) as promising antiproliferative agents for colon cancer [33].



87: R = H, $PR'_3 = PPh_3$
88: R = Br, $PR'_3 = PPh_3$
89: R = Cl, $PR'_3 = PPh_3$
90: R = OMe, $PR'_3 = PPh_3$
91: R = H, PR'_3 = PTA
92: R = Br, PR'_3 = PTA
93: R = Cl, PR'_3 = PTA
94: R = OMe, PR'_3 = PTA

95: R = H, R' = Me
96: R = Br, R' = Me
97: R = Cl, R' = Me
98: R = OMe, R' = Me
99: R = H, R' = IPr
100: R = Br, R' = IPr
101: R = Cl, R' = IPr
102: R = OMe, R' = IPr

Figure 18. Chemical structures of Au(I) hydroxyflavone complexes **87–94** bearing phosphane ligands, and complexes **95–102** featuring N-heterocyclic carbene derivatives, as reported by Mármol et al. [33,34].

A two-step synthesis of 3-OH–F-derivatives followed a slightly changed synthetic path of Gunduz et al. [70] when 2-hydroxyacetophenone was reacted with benzaldehyde or the different para-substituted benzaldehydes in a 1:1 molar ratio under base conditions and a 3 h reflux. The obtained derivatives were further derivatized with propargyl bromide to obtain four new ligands bearing a propargyl ether group. Au(I) complexes **87–94** were synthesized in MeOH after 20 h of stirring obtained ligands with the metal precursor, [AuCl(PR'_3)] (PR'_3 = PPh_3, PTA), at room temperature. The characterization of novel compounds included NMR, IR, and XRD analysis for the OH–F derivative-bearing OMe group,

while their purity was confirmed by EA. Their stability under physiological conditions (in phosphate-buffered saline (PBS) buffer at pH = 7.4 and 37 °C) was confirmed by UV–Vis absorption spectroscopy. The structural optimization of these flavonoid-inspired compounds, known for their pronounced lipophilicity, involved the introduction of a propargyl ether unit followed by coordination with a Au–phosphane moiety. This modification resulted in a well-balanced lipophilic–hydrophilic profile, with improved lipophilicity (log P) values ranging from 0.23 to 1.2.

Prior to the biological study, authors evaluated the interaction of Au(I) species with BSA adding the increasing amounts of **87**–**94** to the BSA solution. Using fluorescence emission spectroscopy, no emission was noticed in the range from 310 to 400 nm for **87**–**94**. In addition, the binding constants and the number of binding sites for each experiment were calculated from fluorescence intensity data, identifying the hydrophobic cavity of site I in subdomain IIA of BSA as the most probable binding location.

Cell culture experiments were performed on the human colorectal adenocarcinoma subline (Caco-2/TC7), as well as on the MCF-7 (breast), HepG2 (liver), and differentiated Caco-2 cells (noncancerous colon model), in the concentration range of 0–100 μM, using auranofin and cisplatin as positive controls. As the literature reports that flavones-based compounds can influence MTT assay, Mármol et al. primarily tested the toxicity of 3-OH–F and its derivatives on undifferentiated Caco-2/TC7 cells using both MTT and SRB assays. Mármol's study combined IC_{50} for four different 3-OH–F ligands obtained by MTT and SRB indicating that IC_{50} values from SRB were 1.2 to 5 times lower in comparison to those obtained by MTT. In addition, the SRB results were more reproducible, making this technique more reliable. In contrast, this type of behavior was not observed for eight Au(I) complexes **87**–**94** at concentrations below 20 mM with the exception of **90** (Table 24). MTT and SRB tests resulted in similar dose–response curves and comparable IC_{50} values. Since all Au(I) complexes **87**–**94** showed a reduced cell proliferation for all cell lines, the study clearly demonstrated the positive impact of metal coordination. Therefore, complexes **88** and **93,** with the strongest anticancer potential and selectivity, emerged as the most promising candidates for further biological evaluations. The first step included the measurement of cyclooxygenase-1 and cyclooxygenase-2 (COX-1/2) activity, keeping in mind the flavones affinity toward cyclooxygenase [71], and the analysis of redox enzymes thioredoxin reductase (TrxR) and glutathione reductase (GR) inhibition. In both experiments, it was confirmed that Au(I) species interact with COX-1/2 and TrxR and GR redox enzymes, proceeding to ROS increase on CaCo-2 cell lines. At the stage when biological targets were identified, the type of a cell death was examined for both complexes **88** and **93**. The experiments revealed that cell death occurred through the intrinsic apoptotic pathway and was accompanied by changes in cell cycle progression. Toxicity evaluation on differentiated Caco-2 cells, used as a model for noncancerous tissue, suggested that flavone-inspired gold complexes **88** and **93** may preferentially target cancer cells over normal differentiated cells, making them promising candidates for cancer treatment.

The same research group expanded the series of Au(I) complexes bearing N-heterocyclic carbene (NHC) derivatives and an OH–F moiety functionalized with a propargyl ether group (Figure 18) [34]. Mármol et al. reported eight [AuCl(NHC)]-type complexes (**95**–**102**), where NHC stands for 1,3-bis(2,6-diisopropylphenyl)imidazolidin-2-ylidene (IPr; $C_{27}H_{38}N_2$) or 1,3-dimethylimidazolidin-2-ylidene (IMe; $C_5H_{10}N_2$). The compounds **95**–**102** were synthesized by reacting four different previously obtained 3-OH–F derivatives with [AuCl(NHC)] in methanol in the presence of two equivalents of KOH as the base. The reaction mixture was stirred for 8 h at room temperature, after which the solvent was evaporated. The pure products were obtained as white, stable solids following a work-up procedure that included the addition of dichloromethane and diethyl ether. The next step

involved a comprehensive characterization of complexes **95–102** using NMR, IR, HRMS, and EA. Subsequently, the shake-flask method combined with UV–Vis spectroscopy was used to determine their distribution coefficients. Based on the results (log P: 0.34–1.96 for IMe; 0.42–3.4 for IPr), the complexes were classified as lipophilic species. Given that chemical stability under physiological conditions is essential for upcoming biological studies, Mármol et al. conducted stability tests in PBS at pH 7.4 and 37 °C over a 24 h period. UV–Vis monitoring of the solutions revealed no spectral changes in the main absorption bands (λ = 210–350 nm), nor any noticeable red or blue shifts. These findings confirmed that complexes **95–102** remain stable under the tested experimental conditions.

Table 24. Cytotoxicity results for reviewed Au(I) **87–94** complexes obtained by linear-type coordination after 72 h treatment using MTT assay on human cell lines undifferentiated Caco-2/TC7, MCF-7 and HepG2 cancer cell lines, and differentiated Caco-2 cells (noncancerous model) compared with auranofin and cisplatin [33].

Compd.	R	PR'_3	IC_{50} (μM)			
			Caco-2/TC7	MCF-7	HepG2	Dif Caco-2
87	H	PPh_3	3.81 ± 1.18	2.08 ± 0.17	32.34 ±4.27	131.30 ± 38.54
88	Br	PPh_3	1.52 ± 0.91	13.87 ± 0.78	3.38 ± 0.07	43.89 ± 0.02
89	Cl	PPh_3	5.34 ± 0.05	8.99 ± 3.89	34.14 ± 5.88	114.38 ± 9.24
90	OMe	PPh_3	4.78 ± 0.62	3.40 ± 0.85	47.97 ± 5.32	75.45 ± 11.28
91	H	PTA	7.68 ± 1.74	18.49 ± 0.90	10.84 ± 0.67	18.25 ± 1.34
92	Br	PTA	6.42 ± 0.35	8.80 ± 3.14	11.25 ± 0.63	24.39 ± 0.86
93	Cl	PTA	2.33 ± 1.26	7.57 ± 0.08	5.88 ± 0.04	25.46 ± 0.66
94	OMe	PTA	5.22 ± 0.43	9.19 ± 2.89	10.70 ± 1.35	25.29 ± 0.60
cisplatin	–	–	37.24 ± 5.15	41.82 ± 0.07	49.85 ± 6.66	151.13 ± 58.12
auranofin	–	–	1.80 ± 0.10	0.77 ± 0.05	0.92 ± 0.08	6.21 ± 0.44

The antiproliferative activity of compounds **95–102** was evaluated on Caco-2 (colon) cells after a 72 h incubation period using the MTT assay in a concentration range of 0–20 μM, with auranofin as a reference drug. Despite their structural similarity to the previously reported series of Au(I) complexes **87–94** with notable anticancer properties, the new series (**95–102**) exhibited only mild to low activity in comparison to auranofin (Table 25). Nevertheless, the presence of the IMe ligand appeared to have a favorable effect, as evidenced by a significant increase in the antiproliferative activity in the corresponding complexes. Overall, the IMe-containing compounds demonstrated a higher cytotoxicity than their IPr analogs, with the exception of complexes **95** and **99**. However, the antiproliferative results as a whole did not indicate sufficient potential to continue the study.

Selected compounds from the **95–102** series exhibited enhanced biological activity against both Gram-positive and Gram-negative bacterial strains (Table 26). Their antimicrobial properties were evaluated using the disk diffusion assay against six strains: *Escherichia coli*, *Pseudomonas aeruginosa*, *Salmonella enterica*, *Enterococcus faecalis*, *Listeria monocytogenes*, *Staphylococcus epidermidis*, and *Staphylococcus aureus*. The assay was conducted following the guidelines of the Clinical and Laboratory Standards Institute (CLSI) [72]. Stock solutions of the compounds were prepared in concentrations ranging from 0 to 100 μM, and bacterial cultures were incubated for 24 h at 37 °C prior to assessing inhibition zones.

Table 25. Cytotoxicity results for reviewed Au(I) **95**–**102** complexes obtained by linear-type coordination and their precursors after 72 h treatment using MTT assay on Caco-2 cells compared to auranofin [34].

Compd.	R	R′	IC_{50} (μM)
[AuCl(IMe)]	–	–	>100
[AuCl(IPr)]	–	–	9.09 ± 3.22
95	H	Me	43.34 ± 5.06
96	Br	Me	23.01 ± 2.42
97	Cl	Me	15.05 ± 3.04
98	OMe	Me	16.33 ± 1.04
99	H	IPr	16.34 ± 2.04
100	Br	IPr	53.85 ± 22.72
101	Cl	IPr	46.15 ± 22.54
102	OMe	IPr	48.22 ± 14.56
auranofin	–	–	1.80 ± 0.10

Table 26. Antimicrobial activity of selected Au(I) complexes bearing N-heterocyclic carbene derivatives after 24 h incubation obtained by disk diffusion assay using phenol as positive control [34].

Bacterial Strain	Inhibition Zone (mm)				
	96	**98**	**100**	**101**	**Phenol**
E. coli 25922	9.04 ± 2.17	-	-	-	23.39 ± 1.26
E. coli 8739	11.10 ± 0.08	-	8.97 ± 0.49	-	22.71 ± 1.37
E. coli 13216	10.95 ± 0.64	-	8.10 ± 0.60	-	20.70 ± 2.97
P. aeruginosa	-	-	-	-	30.48 ± 1.45
S. enterica 25928	8.90 ± 1.56	-	-	-	19.20 ± 0.42
S. enterica 14028	9.39 ± 1.26	-	-	-	27.79 ± 1.11
E. faecalis	12.50 ± 1.41	9.47 ± 1.67	12.10 ± 0.99	10.25 ± 1.41	13.5 ± 2.12
L. monocytogenes	18.50 ± 1.41	14.25 ± 1.06	17.17 ± 0.24	15.33 ± 0.47	16.58 ± 0.12
S. epidermidis	25.05 ± 1.48	17.23 ± 0.87	20.95 ± 0.91	18.06 ± 2.04	22.67 ± 4.49
S. aureus 2593	13.76 ± 0.54	9.70 ± 0.02	12.79 ± 1.11	10.49 ± 1.13	12.05 ± 0.73
S. aureus 13565	16.58 ± 1.63	11.86 ± 0.20	14.03 ± 0.17	12.19 ± 0.88	17.25 ± 3.38

Two compounds, **96** and **100**, were distinguished in the series, demonstrating greater activity in comparison to phenol. Additionally, the authors evaluated the mechanism of action for **96**, relying on estimations of TrxR and dihydrofolate reductase (DHFR) activities, and further supported by SEM. In the case of *Escherichia coli* strain, no inhibition of the TrxR was spotted, but DHFR activity was altered in the presence of **96**. This result insinuated that DHFR had a crucial role in the final antibacterial activity of **96**.

3. Conclusions

3.1. Retrospective View of the Authors

In the current era of medicinal chemistry, naturally inspired compounds play a crucial role in the discovery and design of new therapeutics. Notably, nearly 50% of FDA-approved drugs are structurally related to natural products [5]. In this context, hydroxyflavone (OH–F) scaffolds combined with metal centers have gained attention as promising platforms for the development of anticancer and antimicrobial agents. Across the majority of published studies, a common feature of OH–F was recognized: its broad spectrum of biological activities, ranging from anticancer and antimicrobial to anti-inflammatory, antiviral, antimutagenic, and vasodilatory effects [73].

In our present study, we reviewed more than twenty studies published between 2010 and 2024 that investigated the biological activity of [M(OH–F)] coordination com-

pounds, focusing on their anticancer and/or antimicrobial effects. In total, 102 complexes with various transition metals were described and classified based on their coordination mode (e.g., maltol-like, acetylacetonate, catecholate, and mixed-ligand types).

Importantly, nineteen out of twenty-two studies reported that coordination with metal centers enhanced the biological activity compared to the free ligands, justifying the incorporation of metals into OH–F-based pharmacophores. Only three studies deviated from this trend.

Despite these promising results of [M(OH–F)], their pharmaceutical application remains limited due to poor aqueous solubility. To address this challenge, we propose two key strategies. First, structural modification through the incorporation of nitrogen-containing heterocycles could enhance solubility and ligand versatility, given the prevalence of such moieties in approved drugs. Second, systematic derivatization of the OH–F platform could improve water compatibility and stability under physiological conditions, thus increasing the potential for clinical translation.

In parallel, there is a growing interest in coupling these bioactive metal complexes with biocompatible carriers and delivery matrices (e.g., chitosan, alginate, and gelatin, as well as liposomes, solid lipid nanoparticles (SLNs), and poly(lactic-co-glycolic acid) (PLGA) nanoparticles) to overcome solubility barriers and improve therapeutic outcomes. Natural polymers, lipid-based systems, and hybrid nanostructures are being actively explored for their ability to stabilize coordination compounds and modulate their release under physiological conditions. Incorporating [M(OH–F)] complexes into such delivery systems could significantly expand their biomedical utility, enabling targeted delivery, reduced toxicity, and enhanced bioavailability. These directions represent a promising frontier in medicinal chemistry, where the convergence of natural product-inspired scaffolds and metal coordination continues to unlock new therapeutic opportunities. These systems offer advantages such as controlled release, enhanced bioavailability, and targeted delivery, making them ideal candidates for the administration of coordination compounds. Combining the therapeutic potential of [M(OH–F)] scaffolds with modern drug delivery strategies has great promise for translating these complexes into clinically viable treatments.

The final part of our review addresses several common shortcomings identified in the chemical characterization and biological evaluation of the studied compounds. Some studies lacked comprehensive structural characterization of the newly synthesized complexes, with missing data such as NMR, HRMS, EA, or XRD crystallography. Others showed deviations in the biological testing, including the absence of reference compounds, lack of solubility or stability assessments, or insufficient experimental controls. These gaps can compromise the reliability of the reported biological activity and may lead to misleading conclusions at early stages of drug development and pre-clinical evaluation.

In light of the abovementioned conclusions, we would like to finalize this review by emphasizing the significant biological potential of [M(OH–F)] coordination compounds. With proper structural optimization and fine-tuning, particularly regarding solubility, stability, and target selectivity, these complexes represent promising candidates for further development into clinically relevant anticancer and antimicrobial agents.

3.2. Conclusions and Future Prospects

In this concluding section of our review, we would like to highlight several critical considerations that we believe are essential for ensuring the accuracy, reproducibility, and relevance of biological studies involving metal-based compounds.

From a strictly chemical perspective, the comprehensive structural characterization of newly synthesized compounds is strongly advised. This should definitely include techniques such as NMR spectroscopy (^{1}H and ^{13}C), high-resolution mass spectrometry

(HRMS), infrared spectroscopy (IR), elemental analysis (EA), and X-Ray crystallography (XRD). Only the combined usage of these methods can reliably confirm the chemical structure. Despite the well-established nature of this practice, we still observe cases in the literature where characterization is incomplete, and compounds are directly subjected to biological evaluation.

Furthermore, the stability of the complexes in the culture medium and in the solvent used for cytotoxicity assays must be thoroughly assessed, ideally through ^{1}H NMR monitoring over the incubation period. This is a crucial step, as interactions with biological media and stability under physiological conditions significantly impact the therapeutic potential and reproducibility of results.

Cytotoxicity screening should, where possible, be performed on at least five cancerous and one non-cancerous cell line. This enables the calculation of the selectivity index, which provides valuable insight into the compound's tumor-targeting ability. The choice of a positive control must correspond to the specific tumor type under investigation, and its cytotoxicity should be evaluated under identical experimental conditions rather than cited from the literature to ensure a meaningful comparison.

Therefore, we hope this review offers constructive recommendations that will contribute to more rigorous and informative future studies on metal-based compounds with promising potential in drug development.

Funding: The authors gratefully acknowledge financial support from the European Union HORIZON-MSCA through the MET-EFFECT project under grant No. 101086373, PROMISEANG under grant agreement 101036768 funded from the Bio Based Industries Joint Undertaking (JU), and the Ministry of Science, Technological Development and Innovation of the Republic of Serbia, grant Nos. 451-03-136/2025-03/200288 and 451-03-136/2025-03/200026. The JU-CBE receives support from the European Union's Horizon 2020 research and innovation programme and the Bio Based Industries Consortium.

Data Availability Statement: No new data were created or analyzed in this study.

Conflicts of Interest: Author Ljiljana E. Mihajlović was employed by the company Innovation Center of the Faculty of Chemistry. Author Monica Trif was employed by the company Centre for Innovative Process Engineering (CENTIV) GmbH. The remaining authors declare that the research was conducted in the absence of any commercial or financial relationships that could be construed as a potential conflict of interest.

Abbreviations

3-OH-F	3-hydroxyflavone
4CL	4-coumarate-CoA ligase
5-OH-F	5-hydroxyflavone
A431	human epithelial carcinoma cell line
A549	human lung carcinoma epithelial cells
ATP	adenosine triphosphate
apg	apigenin
Bcl-2	B-cell lymphoma 2
bpy	2,2′-bipyridine
B16F10	murine melanoma, c57bl/6j mouse
BSA	bovine serum albumin
CA	conductometric analysis
Caco-2	human colorectal adenocarcinoma cell line
Caco-2/TC7	human colorectal adenocarcinoma cell subline

C4H	cinnamate-4-hydroxylase
CHI	chalcone isomerase
CHS	chalcone synthase
CDDP	cisplatin, cis-diamminedichloroplatinum(II)
chr	chrysin
CH1	human ovarian carcinoma cell line
COX-1/2	cyclooxygenase-1 and cyclooxygenase-2
CV	cyclic voltammetry
Compd.	compound
DFT	density functional theory
DHFR	dihydrofolate reductase
DIP	4,7-diphenyl-1,10-phenanthroline
DL	Dalton's lymphoma, murine transplantable t-cell lymphoma
DMSO	dimethyl sulfoxide
DNA	deoxyribonucleic acid
EA	elemental analysis
EAC	Ehrlich ascites carcinoma
EB	ethidium bromide
EPR	electron paramagnetic resonance
FaDU	human hypopharyngeal squamous cell carcinoma
FNS	flavone synthase
FS	fluorescence spectroscopy
GR	glutathione reductase
HL-7702	normal human liver cells
HEK293	non-cancerous human embryonic kidney cells
HeLa	human cervical adenocarcinoma cell line
HepG2	human hepatocellular carcinoma cell line
HRMS	high resolution mass spectrometry
HSA	human serum albumin
HT-29	human colorectal adenocarcinoma
HUVECs	human umbilical vein endothelial cells
ICP-AES	coupled plasma atomic emission spectrometry
IMe	1,3-dimethylimidazolidin-2-ylidene
IPr	1,3-bis(2,6-diisopropylphenyl)imidazolidin-2-ylidene
i.p.	intraperitoneally
IR	infrared
iso	isoorientin
Jurkat	human T-lymphocyte
kaemp	kaempferol
K562	human myelogenous leukemia
KG-1	human acute myelogenous leukemia
L	ligand
log P	lipophilicity
LoVo	human colon adenocarcinoma
lut	luteolin
NMR	nuclear magnetic resonance
MCF-7	human hormone-dependant breast adenocarcinoma cell line
MDA-MB-231	human triple-negative breast cancer cell line, highly metastatic
MDA-MB-435S	human metastatic breast cancer cell line
MG63	human osteosarcoma cell line
MMP-9	matrix metalloproteinase-9
mor	morin
MTT	3-(4,5-dimethylthiazol-2-yl)-2,5-diphenyltetrazolium bromide

OH-F	hydroxyflavone
p53	tumor suppressor protein involved in cell cycle regulation and apoptosis
PBS	phosphate-buffered saline
phen	1,10-phenanthroline
PAL	phenylalanine ammonia-lyase
PC3	human prostate adenocarcinoma cell line
PCy3	tricyclohexylphosphine
PPh3	triphenylphosphine
PTA	1,3,5-triaza-7-phosphaadamantane
PXRD	powder X-Ray diffraction analyses
querc	quercetin
rut	rutin
ROS	reactive oxygen species
RPE-1	non-cancerous human retinal pigment epithelial cells immortalized with hTERT
RPMI8226	human myeloma
SEM	scanning electron microscopy
SEM	standard error of the mean
SD	standard deviation
SI	selectivity index
SK-MEL-28	human skin melanoma
SK-OV-3	human ovarian adenocarcinoma
SRB	sulforhodamine B
SW480	human colorectal adenocarcinoma cell line
SW620	human colorectal adenocarcinoma cell line
TA	thermal analysis
tchr	tectochrysin
TEM	transmission electron microscopy
TGA	thermogravimetric analysis
Tf	transferrin
THF	tetrahydrofuran
TLC	thin layer chromatography
TMS	tetramethylsilane
tpa	tris(2-pyridylmethyl)amine
tren	tris(2-aminoethyl)amine
TrxR	thioredoxin reductase
WHO	world health organization
U87	human glioblastoma astrocytoma cell line
UV-Vis	ultraviolet-visible spectroscopy
VEGF	vascular endothelial growth factor
WI-38	human normal lung fibroblast cell line (derived from embryonic lung tissue)
XRD	X-Ray diffraction analysis
χ	magnetic susceptibility

References

1. Cancer. Available online: https://www.who.int/news-room/fact-sheets/detail/cancer (accessed on 30 June 2025).
2. Preisler, H.D. Resistence to cytotoxic therapy: A speculative overview. *Ann. Oncol.* **1995**, *6*, 651–657. [CrossRef] [PubMed]
3. Mansoori, B.; Mohammadi, A.; Davudian, S.; Shirjang, S.; Baradaran, B. The different mechanisms of cancer drug resistance: A brief review. *Adv. Pharm. Bull.* **2017**, *7*, 339–348. [CrossRef] [PubMed]
4. Davies, J.; Davies, D. Origins and evolution of antibiotic resistance. *Microbiol. Mol. Biol. Rev.* **2010**, *74*, 417–433. [CrossRef] [PubMed]
5. Newman, D.J.; Cragg, G.M. Natural products as sources of new drugs over the nearly four decades from 01/1981 to 09/2019. *J. Nat. Prod.* **2020**, *83*, 770–803. [CrossRef] [PubMed]
6. Malešev, D.; Kuntić, V. Investigation of metal–flavonoid chelates and the determination of flavonoids via metal-flavonoid complexing reactions. *J. Serb. Chem. Soc.* **2007**, *72*, 921–939. [CrossRef]

7. Guo, M.; Perez, C.; Wei, Y.; Rapoza, E.; Su, G.; Bou-Abdallah, F.; Chasteen, N.D. Iron-binding properties of plant polyphenols and their biological significance. *Dalton Trans.* **2007**, *2007*, 4951–4961. [CrossRef] [PubMed]
8. Lou, H.; Hu, L.; Lu, H.; Wei, T.; Chen, Q. Metabolic Engineering of Microbial Cell Factories for Biosynthesis of Flavonoids: A Review. *Molecules* **2021**, *26*, 4522. [CrossRef] [PubMed]
9. Kasprzak, M.M.; Erxleben, A.; Ochocki, J. Properties and applications of flavonoid metal complexes. *RSC Adv.* **2015**, *5*, 45853–45877. [CrossRef]
10. Agati, G.; Azzarello, E.; Pollastri, S.; Tattini, M. Flavonoids as antioxidants in plants: Location and functional significance. *Plant Sci.* **2012**, *196*, 67–76. [CrossRef] [PubMed]
11. Treutter, D. Significance of flavonoids in plant resistance: A review. *Plant Biol.* **2005**, *7*, 581–591. [CrossRef] [PubMed]
12. Hernández, I.; Alegre, L.; Van Breusegem, F.; Munné-Bosch, S. How relevant are flavonoids as antioxidants in plants? *Trends Plant Sci.* **2009**, *14*, 125–132. [CrossRef] [PubMed]
13. Buer, C.S.; Imin, N.; Djordjevic, M.A. Flavonoids: New roles for old molecules. *J. Integr. Plant Biol.* **2010**, *52*, 98–111. [CrossRef] [PubMed]
14. Cotelle, N.; Bernier, J.-L.; Catteau, J.-P.; Pommery, J.; Wallet, J.-C.; Gaydou, E.M. Antioxidant properties of hydroxy-flavones. *Free Radic. Biol. Med.* **1996**, *20*, 35–43. [CrossRef] [PubMed]
15. Magnani, L.; Gaydou, E.M.; Hubaud, J.C. Spectrophotometric measurement of antioxidant properties of flavones and flavonols against superoxide anion. *Anal. Chim. Acta* **2000**, *411*, 209–216. [CrossRef]
16. Lemanska, K.; Szymusiak, H.; Tyrakowska, B.; Zielinsky, R.; Soffers, E.M.F.; Rietjens, I.M.C.M. The influence of pH on antioxidant properties and the mechanism of antioxidant action of hydrxiflavones. *Free Radic Biol. Med.* **2001**, *31*, 869–881. [CrossRef]
17. de Souza, R.F.V.; Sussuchi, E.M.; De Giovani, W.F. Synthesis, Electrochemical, Spectral, and Antioxidant Properties of Complexes of Flavonoids with Metal Ions. *Synth. React. Inorg. Met.-Org. Chem.* **2003**, *33*, 1125–1144. [CrossRef]
18. Lewandowski, W.; Lewandowska, H.; Golonko, A.; Świderski, G.; Świsłocka, R.; Kalinowska, M. Correlations between molecular structure and biological activity in "logical series" of dietary chromone derivatives. *PLoS ONE* **2020**, *15*, e0229477. [CrossRef] [PubMed]
19. Leonte, D.; Ungureanu, D.; Zaharia, V. Flavones and Related Compounds: Synthesis and Biological Activity. *Molecules* **2023**, *28*, 6528. [CrossRef] [PubMed]
20. Fotsis, T.; Pepper, M.S.; Montesano, R.; Aktas, E.; Breit, S.; Schweigerer, L.; Rasku, S.; Wahala, K.; Adlercreutz, H. Phytoestrogens and inhibition of angiogenesis. *Baillieres Clin. Endocrinol. Metab.* **1998**, *12*, 649–666. [CrossRef] [PubMed]
21. Kim, M.H. Flavonoids Inhibit VEGF/bFGF-Induced Angiogenesis In Vitro by Inhibiting the Matrix-Degrading Proteases. *J. Cell. Biochem.* **2003**, *89*, 529–538. [CrossRef] [PubMed]
22. Sanderson, J.T.; Hordijk, J.; Denison, M.S.; Springsteel, M.F.; Nantz, M.H.; van den Berg, M. Induction and Inhibition of Aromatase (CYP19) Activity by Natural and Synthetic Flavonoid Compounds in H295R Human Adrenocortical Carcinoma Cells. *Toxicol. Sci.* **2004**, *82*, 70–79. [CrossRef] [PubMed]
23. Holder, S.; Zemskova, M.; Zhang, C.; Tabrizizad, M.; Bremer, R.; Neidigh, J.W.; Lilly, M.B. Characterization of a potent and selective small-molecule inhibitor of the PIM1 kinase. *Mol. Cancer Ther.* **2007**, *6*, 163–172. [CrossRef] [PubMed]
24. Loa, J.; Chow, P.; Zhang, K. Studies of structure–activity relationship on plant polyphenol-induced suppression of human liver cancer cells. *Cancer Chemother. Pharmacol.* **2009**, *63*, 1007–1016. [CrossRef] [PubMed]
25. Math, H.H.; Kumar, R.S.; Chakraborty, B.; Almansour, A.I.; Perumal, K.; Kantli, G.B.; Nayaka, S. Antimicrobial Efficacy of 7-hydroxyflavone Derived from Amycolatopsis sp. HSN-02 and Its Biocontrol Potential on Cercospora Leaf Spot Disease in Tomato Plants. *Antibiotics* **2023**, *12*, 1175. [CrossRef] [PubMed]
26. Torres-Piedra, M.; Ortiz-Andrade, R.; Villalobos-Molina, R.; Singh, N.; Medina-Franco, J.L.; Webster, S.P.; Binnie, M.; Navarrete-Vázquez, G.; Estrada-Soto, S. A comparative study of flavonoid analogues on streptozotocinenicotinamide induced diabetic rats: Quercetin as a potential antidiabetic agent acting via 11b–Hydroxysteroid dehydrogenase type 1 inhibition. *Eur. J. Med. Chem.* **2010**, *45*, 2606–2612. [CrossRef] [PubMed]
27. Pillai, S.I.; Subramanian, S.P.; Kandaswamy, M. A novel insulin mimetic vanadiumeflavonol complex: Synthesis, characterization and in vivo evaluation in STZ-induced rats. *Eur. J. Med. Chem.* **2013**, *63*, 109–117. [CrossRef] [PubMed]
28. Calderone, V.; Chericoni, S.; Martinelli, C.; Testai, L.; Nardi, A.; Morelli, I.; Breschi, M.C.; Martinotti, E. Vasorelaxing effects of flavonoids: Investigation on the possible involvement of potassium channels. *Naunyn-Schmiedeberg's Arch. Pharmacol.* **2004**, *370*, 290–298. [CrossRef] [PubMed]
29. Liu, X.; Chan, C.-B.; Jang, S.-W.; Pradoldej, S.; Huang, J.; He, K.; Phun, L.H.; France, S.; Xiao, G.; Jia, Y.; et al. A Synthetic 7,8-hihydroxyflavone Derivative Promotes Neurogenesis and Exhibits Potent Antidepressant Effect. *J. Med. Chem.* **2010**, *53*, 8274–8286. [CrossRef] [PubMed]
30. Tasdemir, D.; Kaiser, M.; Brun, R.; Yardley, V.; Schmidt, T.J.; Tosun, F.; Rüedi, P. Antitrypanosomal and Antileishmanial Activities of Flavonoids and Their Analogues: In Vitro, In Vivo, Structure-Activity Relationship, and Quantitative Structure-Activity Relationship Studies. *Antimicrob. Agents Chemother.* **2006**, *50*, 1352–1364. [CrossRef] [PubMed]

31. Grazul, M.; Budzisz, E. Biological activity of metal ions complexes of chromones, coumarins and flavones. *Coord. Chem. Rev.* **2009**, *253*, 2588–2598. [CrossRef]
32. Yang, A.; Liu, C.; Zhang, H.; Wu, J.; Shen, R.; Kou, X. A multifunctional anti-AD approach: Design, synthesis, X-ray crystal structure, biological evaluation and molecular docking of chrysin derivatives. *Eur. J. Med. Chem.* **2022**, *233*, 114216–114232. [CrossRef] [PubMed]
33. Mármol, I.; Castellnou, P.; Alvarez, R.; Gimeno, M.C.; Rodríguez-Yoldi, M.J.; Cerrada, E. Alkynyl gold(I) complexes derived from 3-hydroxyflavones as multi-targeted drugs against colon cancer. *Eur. J. Med. Chem.* **2019**, *183*, 111661. [CrossRef] [PubMed]
34. Mármol, I.; Quero, J.; Azcárate, P.; Atrián-Blasco, E.; Ramos, C.; Santos, J.; Gimeno, M.C.; Rodríguez-Yoldi, M.J.; Cerrada, E. Biological activity of NHC-gold-alkynyl complexes derived from 3-hydroxyflavones. *Pharmaceutics* **2022**, *14*, 2064. [CrossRef] [PubMed]
35. Andrades Ikeda, N.E.; Novak, E.M.; Maria, D.A.; Velosa, A.S.; Silva Pereira, R.M. Synthesis, characterization and biological evaluation of rutin–zinc(II) flavonoid-metal complex. *Chem.-Biol. Interact.* **2015**, *239*, 184–191. [CrossRef] [PubMed]
36. Wang, X.; He, S.; Yuan, L.; Deng, H.; Zhang, Z. Synthesis, structure characterization, and antioxidant and antibacterial activity study of iso-orientin–zinc complex. *J. Agric. Food Chem.* **2021**, *69*, 3952–3964. [CrossRef] [PubMed]
37. Dell'Anna, M.M.; Censi, V.; Carrozzini, B.; Caliandro, R.; Denora, N.; Franco, M.; Veclani, D.; Melchior, A.; Tolazzi, M.; Mastrorilli, P. Triphenylphosphane Pt(II) complexes containing biologically active natural polyphenols: Synthesis, crystal structure, molecular modeling and cytotoxic studies. *J. Inorg. Biochem.* **2016**, *163*, 346–361. [CrossRef] [PubMed]
38. Raza, A.; Xu, X.; Xia, L.; Xia, C.; Tang, J.; Ouyang, Z. Quercetin-Iron Complex: Synthesis, Characterization, Antioxidant, DNA Binding, DNA Cleavage, and Antibacterial Activity Studies. *J. Fluoresc.* **2016**, *26*, 2023–2031. [CrossRef] [PubMed]
39. Repac Antić, D.; Parčina, M.; Gobin, I.; Petković Didović, M. Chelation in Antibacterial Drugs: From Nitroxoline to Cefiderocol and Beyond. *Antibiotics* **2022**, *11*, 1105. [CrossRef] [PubMed]
40. Sahyon, H.A.; Althobaiti, F.; Ramadan, A.E.-M.M.; Fathy, A.M. Quercetin—Based rhodium(III) complex: Synthesis, characterization and diverse biological potentials. *J. Mol. Struct.* **2022**, *1257*, 132584. [CrossRef]
41. Singh, A.K.; Saxena, G.; Sahabjada; Arshad, M. Synthesis, characterization and biological evaluation of ruthenium flavanol complexes against breast cancer. *Spectrochim. Acta Part A Mol. Biomol. Spectrosc.* **2017**, *180*, 97–104. [CrossRef] [PubMed]
42. Prajapati, R.; Kumar Dubey, S.; Gaur, R.; Koiri, R.K.; Maurya, B.K.; Trigun, S.K.; Mishra, L. Structural characterization and cytotoxicity studies of ruthenium(II)–dmso–chloro complexes of chalcone and flavone derivatives. *Polyhedron* **2010**, *29*, 1055–1061. [CrossRef]
43. Sava, G.; Bergamo, A. Ruthenium-based compounds and tumour growth control (review). *Int. J. Oncol.* **2000**, *17*, 353–365. [CrossRef] [PubMed]
44. Alessio, E.; Balducci, G.; Lutman, A.; Mestroni, G.; Calligaris, M.; Attia, W.M. Synthesis and characterization of two new classes of ruthenium(III)-sulfoxide complexes with nitrogen donor ligands (L): Na[trans-$RuCl_4(R_2SO)(L)$] and mer, cis-$RuCl_3(R_2SO)(R_2SO)(L)$. The crystal structure of Na[trans-$RuCl_4$(DMSO)(NH_3)] · 2DMSO, Na[trans-$RuCl_4$(DMSO)(Im)] · H_2O, Me_2CO (Im = imidazole) and mer, cis-$RuCl_3$(DMSO)(DMSO)(NH_3). *Inorg. Chim. Acta* **1993**, *203*, 205–217. [CrossRef]
45. Gantsho, V.L.; Dotou, M.; Jakubaszek, M.; Goud, B.; Gasser, G.; Vissera, H.G.; Schutte-Smith, M. Synthesis, characterization, kinetic investigation and biological evaluation of Re(I) di- and tricarbonyl complexes with tertiary phosphine ligands. *Dalton Trans.* **2020**, *49*, 35–46. [CrossRef] [PubMed]
46. Kurzwernhart, A.; Kandioller, W.; Bartel, C.; Bächler, S.; Trondl, R.; Mühlgassner, G.; Jakupec, M.A.; Arion, V.B.; Marko, M.; Keppler, B.K.; et al. Targeting the DNA-topoisomerase complex in a double-strike approach with a topoisomerase inhibiting moiety and covalent DNA binder. *Chem. Commun.* **2012**, *48*, 4839–4841. [CrossRef] [PubMed]
47. Kurzwernhart, A.; Kandioller, W.; Bächler, S.; Bartel, C.; Martic, S.; Buczkowska, M.; Mühlgassner, G.; Jakupec, M.A.; Kraatz, H.-B.; Bednarski, P.J.; et al. Structure-Activity Relationships of Targeted $Ru^{II}(\eta^6$-*p*-Cymene) Anticancer Complexes with Flavonol-Derived Ligands. *J. Med. Chem.* **2012**, *55*, 10512–10522. [CrossRef] [PubMed]
48. Kurzwernhart, A.; Kandioller, W.; Enyedy, É.A.; Novak, M.; Jakupec, M.A.; Keppler, B.K.; Hartinger, C.G. 3-Hydroxyflavones vs. 3-hydroxyquinolinones: Structure–activity relationships and stability studies on Ru^{II}(arene) anticancer complexes with biologically active ligands. *Dalton Trans.* **2013**, *42*, 6193–6202. [CrossRef] [PubMed]
49. Kurzwernhart, A.; Mokesch, S.; Klapproth, E.; Adib-Razavi, M.S.; Jakupec, M.A.; Hartinger, C.G.; Kandioller, W.; Keppler, B.K. Flavonoid-based organometallics with different metal centers—Investigations of the effects on reactivity and cytotoxicity. *Eur. J. Inorg. Chem.* **2016**, *2016*, 240–246. [CrossRef]
50. Zahirović, A.; Kahrović, E.; Cindrić, M.; Kraljević Pavelić, S.; Hukić, M.; Harej, A.; Turkušić, E. Heteroleptic ruthenium bioflavonoid complexes: From synthesis to in vitro biological activity. *J. Coord. Chem.* **2017**, *70*, 4030–4053. [CrossRef]
51. Gençkal, H.M.; Erkisa, M.; Alper, P.; Sahin, S.; Ulukaya, E.; Ari, F. Mixed ligand complexes of Co(II), Ni(II) and Cu(II) with quercetin and diimine ligands: Synthesis, characterization, anti-cancer and anti-oxidant activity. *J. Biol. Inorg. Chem.* **2020**, *25*, 161–177. [CrossRef] [PubMed]

52. Wang, Q.; Huang, M.; Huang, Y.; Zhang, J.-S.; Zhou, G.-F.; Zeng, R.-Q.; Yang, X.-B. Synthesis, characterization, DNA interaction, and antitumor activities of mixed-ligand metal complexes of kaempferol and 1,10-phenanthroline/2,2′-bipyridine. *Med. Chem. Res.* **2014**, *23*, 2659–2666. [CrossRef]
53. Kozsup, M.; Zhou, X.Q.; Farkas, E.; Bényei, A.C.; Bonnet, S.; Patonay, T. (the late); Kónya, K.; Buglyó, P. Synthesis, characterization and cytotoxicity studies of Co(III)-flavonolato complexes. *J. Inorg. Biochem.* **2021**, *217*, 111382. [CrossRef] [PubMed]
54. Sodhi, R.K.; Paul, S. An overview of metal acetylacetonates: Developing areas/routes to new materials and applications in organic syntheses. *Catal. Surv. Asia* **2018**, *22*, 31–62. [CrossRef]
55. Munteanu, A.-C.; Notaro, A.; Jakubaszek, M.; Cowell, J.; Tharaud, M.; Goud, B.; Uivarosi, V.; Gasser, G. Synthesis, characterization, cytotoxic activity, and metabolic studies of ruthenium(II) polypyridyl complexes containing flavonoid ligands. *Inorg. Chem.* **2020**, *59*, 4424–4434. [CrossRef] [PubMed]
56. Munteanu, A.-C.; Musat, M.G.; Mihaila, M.; Badea, M.; Olar, R.; Nitulescu, G.M.; Rădulescu, F.Ș.; Brasoveanu, L.I.; Uivarosi, V. New heteroleptic lanthanide complexes as multimodal drugs: Cytotoxicity studies, apoptosis, cell cycle analysis, DNA interactions, and protein binding. *Appl. Organomet. Chem.* **2020**, e6062. [CrossRef]
57. Marques, J.; Silva, A.M.S.; Marques, M.P.M.; Braga, S.S. Ruthenium(II) trithiacyclononane complexes of 7,3′,4′-trihydroxyflavone, chrysin and tectochrysin: Synthesis, characterisation, and cytotoxic evaluation. *Inorg. Chim. Acta* **2019**, *488*, 71–79. [CrossRef]
58. Marques, J.; Fernandes, J.A.; Almeida Paz, F.A.; Marques, M.P.M.; Braga, S.S. Isolation, crystal structure, and cytotoxicity on osteosarcoma of a ruthenium(III) complex with coordinated acetonitrile. *J. Coord. Chem.* **2012**, *65*, 2489–2499. [CrossRef]
59. Naso, L.G.; Lezama, L.; Valcarcel, M.; Salado, C.; Villacé, P.; Kortazar, D.; Ferrer, E.G.; Williams, P.A.M. Bovine serum albumin binding, antioxidant and anticancer properties of an oxidovanadium(IV) complex with luteolin. *J. Inorg. Biochem.* **2016**, *157*, 80–93. [CrossRef] [PubMed]
60. Lopez-Lazaro, M. Distribution and biological activities of the flavonoid luteolin. *Mini Rev. Med. Chem.* **2009**, *9*, 31–59. [CrossRef] [PubMed]
61. Ferrer, E.G.; Salinas, M.V.; Correa, M.J.; Naso, L.; Barrio, D.A.; Etcheverry, S.B.; Lezama, L.; Rojo, T.; Williams, P.A.M. Synthesis, characterization, antitumoral and osteogenic activities of quercetin vanadyl(IV) complexes. *J. Biol. Inorg. Chem.* **2006**, *11*, 791–801. [CrossRef] [PubMed]
62. Etcheverry, S.B.; Ferrer, E.G.; Naso, L.; Rivadeneira, J.; Salinas, V.; Williams, P.A.M. Antioxidant effects of the VO(IV) hesperidin complex and its role in cancer chemoprevention. *J. Biol. Inorg. Chem.* **2007**, *13*, 435–447. [CrossRef] [PubMed]
63. Islas, M.S.; Naso, L.G.; Lezama, L.; Valcarcel, M.; Salado, C.; Roura-Ferrer, M.; Ferrer, E.G.; Williams, P.A.M. Insights into the mechanisms underlying the antitumor activity of an oxidovanadium(IV) compound with the antioxidant naringenin. Albumin binding studies. *J. Inorg. Biochem.* **2015**, *149*, 12–24. [CrossRef] [PubMed]
64. Seelinger, G.; Merfort, I.; Wölfle, U.; Schempp, C.M. Anti-carcinogenic effects of the flavonoid luteolin. *Molecules* **2008**, *13*, 2628–2651. [CrossRef] [PubMed]
65. Sharfalddin, A.A.; Al-Younis, I.M.; Mohammed, H.A.; Dhahri, M.; Mouffouk, F.; Abu Ali, H.; Anwar, M.J.; Qureshi, K.A.; Hussien, M.A.; Alghrably, M. Therapeutic Properties of Vanadium Complexes. *Inorganics* **2022**, *10*, 244. [CrossRef]
66. Deng, S.-P.; Yang, Y.-L.; Cheng, X.-X.; Li, W.-R.; Cai, J.-Y. Synthesis, spectroscopic study and radical scavenging activity of kaempferol derivatives: Enhanced water solubility and antioxidant activity. *Int. J. Mol. Sci.* **2019**, *20*, 975. [CrossRef] [PubMed]
67. Tu, L.-Y.; Pi, J.; Jin, H.; Cai, J.-Y.; Deng, S.-P. Synthesis, characterization and anticancer activity of kaempferol–zinc(II) complex. *Bioorg. Med. Chem. Lett.* **2016**, *26*, 2730–2734. [CrossRef] [PubMed]
68. Liu, L.; Xu, K.; Wang, H.; Tan, P.K.J.; Fan, W.; Venkatraman, S.S.; Li, L.; Yang, Y.-Y. Self-assembled cationic peptide nanoparticles as an efficient antimicrobial agent. *Nat. Nanotechnol.* **2009**, *4*, 457–463. [CrossRef] [PubMed]
69. Yuan, L.; Wang, Y.; Wang, J.; Xiao, H.; Liu, X. Additive effect of zinc oxide nanoparticles and isoorientin on apoptosis in human hepatoma cell line. *Toxicol. Lett.* **2014**, *225*, 294–304. [CrossRef] [PubMed]
70. Gunduz, S.; Goren, A.C.; Ozturk, T. Syntheses of 3-hydroxyflavones. *Org. Lett.* **2012**, *14*, 1576–1579. [CrossRef] [PubMed]
71. Meshram, R.J.; Bagul, K.T.; Pawnikar, S.P.; Barage, S.H.; Kolte, B.S.; Gacche, R.N. Known compounds and new lessons: Structural and electronic basis of flavonoid-based bioactivities. *J. Biomol. Struct. Dyn.* **2020**, *38*, 1168–1184. [CrossRef] [PubMed]
72. Clinical and Laboratory Standards Institute (CLSI). *Performance Standards for Antimicrobial Disk Susceptibility Tests*; Approved Standard; CLSI: Wayne, PA, USA, 2012.
73. Samsonowicz, M.; Regulska, E.; Kalinowska, M. Hydroxyflavone metal complexes—Molecular structure, antioxidant activity and biological effects. *Chem. Biol. Interact.* **2017**, *273*, 245–256. [CrossRef] [PubMed]

Disclaimer/Publisher's Note: The statements, opinions and data contained in all publications are solely those of the individual author(s) and contributor(s) and not of MDPI and/or the editor(s). MDPI and/or the editor(s) disclaim responsibility for any injury to people or property resulting from any ideas, methods, instructions or products referred to in the content.